

Two-dimensional Particle-in-Cell simulations of axisymmetric black hole magnetospheres

KOUCIHI HIROTANI ¹, RUBEN KRASNOPOLSKY ¹, HSIEN SHANG (尚賢) ¹,
KEN-ICHI NISHIKAWA ², AND MICHAEL WATSON ³

¹*Institute of Astronomy and Astrophysics, Academia Sinica, Taipei 10617, Taiwan, R.O.C.*

²*Department of Physics, Chemistry and Mathematics, Alabama A&M University, Huntsville, AL 35811, USA*

³*Department of Physics, Fisk University, 1000 17th Ave North, Nashville, TN 37208, USA*

(Accepted December 15, 2020)

ABSTRACT

We investigate the temporal evolution of an axisymmetric magnetosphere around a rapidly rotating, stellar-mass black hole, applying a two-dimensional particle-in-cell simulation scheme. Adopting a homogeneous pair production, and assuming that the mass accretion rate is much less than the Eddington limit, we find that the black hole’s rotational energy is preferentially extracted from the middle latitudes, and that this outward energy flux exhibits an enhancement that lasts approximately 160 dynamical time scales. It is demonstrated that the magnetohydrodynamic approximations cannot be justified in such a magnetically-dominated magnetosphere, because the Ohm’s law completely breaks down, and because the charge-separated electron-positron plasmas are highly non-neutral. An implication is given regarding the collimation of relativistic jets.

Keywords: acceleration of particles — magnetic fields — methods: analytical — methods: numerical stars: black holes

1. INTRODUCTION

It is commonly accepted that every active galaxy harbors a super-massive black hole (BH) in its center (Ferrarese et al. 1996; Larkin & McLaughlin 2016; Kormendy & Ho 2013). A likely mechanism for powering their relativistic jets is the release of the rotational energy of the BHs (Blandford & Znajek 1977), which is referred to as the Blandford-Znajek (BZ) process, as demonstrated by general-relativistic (GR)

magnetohydrodynamic simulations (Koide et al. 2002; McKinney et al. 2012). In the polar region of a BH magnetosphere, centrifugal force prevents accretion toward the rotation axis and a high vacuum is maintained (Hirose et al. 2004). In this nearly vacuum BH magnetosphere, electrons and positrons (e^{\pm} ’s) are supplied via the collisions of MeV photons emitted from the equatorial, advection-dominated accretion flow (ADAF) (Ichimaru 1977; Narayan & Yi 1994). Particularly, when the mass accretion rate is much less than the Eddington rate, the collisions can no longer sustain a force-

free magnetosphere (Levinson & Rieger 2011). In such a charge-starved magnetosphere, an electric field appears along the magnetic field lines. In this vacuum gap, a portion of the BZ flux is dissipated as particle acceleration and radiation (Beskin et al. 1992; Hirotani & Okamoto 1998; Neronov & Aharonian 2007; Hirotani & Pu 2016). Such a highly vacuum BH magnetosphere has been investigated by the particle-in-cell (PIC) scheme one-dimensionally along a radial magnetic field line (Levinson & Cerutti 2018; Chen et al. 2018; Chen & Yuan 2020; Kisaka et al. 2020), and two-dimensionally in the poloidal plane (Parfrey et al. 2019; Crinquand et al. 2020). In the present paper, adopting a fixed magnetic field in the poloidal plane, we perform a two-dimensional, axisymmetric PIC simulation around a stellar-mass BH. We will examine the temporal evolution of the poloidal components of the electric field, toroidal component of the magnetic field, and the distribution functions of the electrons and positrons that are created and accelerated within the BH magnetosphere.

After describing the background spacetime in § 2.1, we consider the initial conditions of the PIC simulation in § 2. Then we present the results of our 2-D GR PIC simulation in § 3, demonstrating that the magnetohydrodynamic (MHD) approximations totally break down in the vicinity (i.e., at the jet-launching region) of rotating BHs that accrete plasmas at much lower rate than the Eddington rate. In the present paper we focus on a set of astrophysical cases, as described in § 3.5. Code testing cases, including comparison with exact solutions (e.g., development of the electromagnetic field in a plasma-free spacetime, or propagations of charged particles in a fixed electromagnetic field) have been performed, but will be deferred to subsequent papers. Finally, in § 4 we discuss the implication of astrophysical applications to the very-long-baseline-interferometric

(VLBI) observations of supermassive BHs in the center of low-luminosity active galactic nuclei.

2. STATIONARY MAGNETOSPHERE

Let us begin with the stationary solution of the electromagnetic fields in a magnetosphere of a rotating black hole. We will use this stationary solution as the initial condition of time-dependent particle-in-cell (PIC) simulations. Throughout the present paper, we consider two-dimensional structure of the BH magnetosphere in which electrons and positrons are created and accelerated, assuming axisymmetry with respect to the rotation axis of the BH.

2.1. Background geometry

Around a rotating, non-charged BH, the background geometry is described by the Kerr metric (Bardeen 1970). In the Boyer-Lindquist coordinates (Boyer & Lindquist 1967), the line element can be expressed as

$$ds^2 = g_{tt}dt^2 + 2g_{t\varphi}dtd\varphi + g_{\varphi\varphi}d\varphi^2 + g_{rr}dr^2 + g_{\theta\theta}d\theta^2, \quad (1)$$

where

$$g_{tt} \equiv -\frac{\Delta - a^2 \sin^2 \theta}{\Sigma}, \quad g_{t\varphi} \equiv -\frac{2Mar \sin^2 \theta}{\Sigma}, \quad (2)$$

$$g_{\varphi\varphi} \equiv \frac{A \sin^2 \theta}{\Sigma}, \quad g_{rr} \equiv \frac{\Sigma}{\Delta}, \quad g_{\theta\theta} \equiv \Sigma; \quad (3)$$

$\Delta \equiv r^2 - 2Mr + a^2$, $\Sigma \equiv r^2 + a^2 \cos^2 \theta$, $A \equiv (r^2 + a^2)^2 - \Delta a^2 \sin^2 \theta$. In equations (1)–(3), we adopt the geometrized unit, putting $c = G = 1$, where c and G denote the speed of light and the gravitational constant. The horizon radius, $r_H \equiv M + \sqrt{M^2 - a^2}$, is obtained by $\Delta = 0$, where M corresponds to the gravitational radius. The spin parameter becomes $a = M$ for a maximally rotating BH, and $a = 0$ for a non-rotating BH.

2.2. The Zero Angular Momentum Observer (ZAMO)

As a fiducial observer, let us introduce the Zero Angular Momentum Observer (ZAMO), who is static in the poloidal plane (r, θ) but rotates around the BH at the same angular frequency as the spacetime frame dragging frequency, $\omega \equiv -g_{t\varphi}/g_{\varphi\varphi}$. The tetrad of ZAMO reads

$$\tilde{\mathbf{e}}_{(\hat{t})} = \alpha^{-1}(\mathbf{e}_{(t)} + \omega \mathbf{e}_{(\varphi)}), \quad (4)$$

$$\tilde{\mathbf{e}}_{(\hat{r})} = \sqrt{\frac{\Delta}{\Sigma}} \mathbf{e}_{(r)}, \quad (5)$$

$$\tilde{\mathbf{e}}_{(\hat{\theta})} = \frac{1}{\sqrt{\Sigma}} \mathbf{e}_{(\theta)}, \quad (6)$$

$$\tilde{\mathbf{e}}_{(\hat{\varphi})} = \frac{1}{\sqrt{g_{\varphi\varphi}}} \mathbf{e}_{(\varphi)}, \quad (7)$$

where

$$\alpha \equiv \frac{d\tau}{dt} = \frac{\rho_w}{\sqrt{g_{\varphi\varphi}}} = \sqrt{\frac{\Delta\Sigma}{A}} \quad (8)$$

denotes the lapse; $d\tau$ refers to the ZAMO proper time. The tilde ($\tilde{}$) represents a ZAMO-measured quantity and the caret ($\hat{}$) does that the component is projected on an orthonormal basis. At the horizon we have $\alpha = 0$, while away from the BH we have $\alpha = 1$. The coordinate bases are defined as

$$\mathbf{e}_{(t)} = \partial_t, \quad \mathbf{e}_{(r)} = \partial_r, \quad \mathbf{e}_{(\theta)} = \partial_\theta, \quad \mathbf{e}_{(\varphi)} = \partial_\varphi. \quad (9)$$

We use the ZAMO to solve the electromagnetic fields in a stationary magnetosphere (§ 2.3), as well as to present the current densities (figs. 8 & 9) and the particle distribution functions (figs. 10 & 11) in a non-stationary magnetosphere (§ 3).

2.3. Gauss's and Biot-Savart laws

To describe the stationary electromagnetic field, we should simultaneously solve the Gauss's law and the Biot & Savart law. The expressions of these two laws are derived in the Appendix B. For convenience, we replace the independent variable r with the so-called ‘‘tortoise

coordinate’’, r_* . It is defined by

$$\frac{dr_*}{dr} = \frac{r^2 + a^2}{\Delta}. \quad (10)$$

In this coordinate, the horizon corresponds to $r_* \rightarrow -\infty$. At large distances, $dr_*/dr \rightarrow 1$.

What is more, to avoid the singular behaviour due to the $\csc\theta$ factors in the Gauss's law (B31) and the Biot and Savart law (B33) at the poles (i.e., at $\theta = 0$ and π), we introduce a new meridional variable, $y \equiv 1 - \cos\theta$. Adopting this y coordinate, we obtain

$$\frac{1}{\sin\theta} \frac{\partial}{\partial\theta} = \frac{\partial}{\partial y} \quad (11)$$

To avoid the change of the type of the second-order partial differential equation (specifically, the Biot and Savart law) at the static limit, we replace the electro-static potential A_t with the ZAMO-measured value, $A_{\hat{t}}$. The tetrad of ZAMO (eqs. [4]–[7]) gives

$$A_t = \alpha A_{\hat{t}} - \omega A_\varphi \quad (12)$$

and

$$A_\varphi = \sqrt{g_{\varphi\varphi}} A_{\hat{\varphi}}. \quad (13)$$

Using $A_{\hat{t}}$, A_φ , r_* and y , the Biot and Savart law (eq. [B33]) can be rewritten as

$$\begin{aligned} & -\frac{\Delta\Sigma}{A} \frac{\partial^2 A_\varphi}{\partial r_*^2} + C_1 \frac{\partial A_\varphi}{\partial r_*} - \frac{\Delta^2 \Sigma \sin^2 \theta}{(r^2 + a^2)^2 A} \frac{\partial^2 A_\varphi}{\partial y^2} \\ & + \left(\frac{\Delta}{r^2 + a^2} \right)^2 \frac{4Ma^2 r \sin^2 \theta \cos \theta}{\Sigma A} \frac{\partial A_\varphi}{\partial y} + C_0 A_\varphi \\ & + \frac{2Mar \sin^2 \theta}{\Sigma} \frac{\partial^2}{\partial r_*^2} (\alpha A_{\hat{t}}) + C_2 \frac{\partial}{\partial r_*} (\alpha A_{\hat{t}}) \\ & + \frac{2Mar \Delta \sin^2 \theta}{(r^2 + a^2)^2 \Sigma} \frac{\partial^2}{\partial y^2} (\alpha A_{\hat{t}}) \\ & + \frac{4Mar \Delta \sin^2 \theta \cos \theta}{(r^2 + a^2) \Sigma^2} \frac{\partial}{\partial y} (\alpha A_{\hat{t}}) \\ & = 4\pi \left(\frac{\Delta}{r^2 + a^2} \right)^2 \Sigma \sin^2 \theta \cdot J^\varphi, \end{aligned} \quad (14)$$

where

$$C_0 \equiv -\frac{2Mar\Delta \sin^2 \theta}{(r^2 + a^2)^2 \Sigma} \left\{ \Delta(\partial_r^2 \omega) + \left[\frac{(r^2 - a^2 \cos^2 \theta)\Delta}{r\Sigma} - \frac{2M(r^2 - a^2)}{r^2 + a^2} \right] (\partial_r \omega) + \sin^2 \theta (\partial_y^2 \omega) + \frac{2(r^2 + a^2) \cos \theta}{\Sigma} (\partial_y \omega) \right\}, \quad (15)$$

$$C_1 \equiv \frac{2\Delta}{(r^2 + a^2)^2 \Sigma^2} \times \left[-(r - M)(r^2 + a^2)\Sigma + \frac{(r^2 + a^2)\Sigma}{A} C_3 + (\Delta - a^2 \sin^2 \theta) r a^2 \sin^2 \theta + \frac{4M^2 a^4 r^3 \sin^4 \theta}{A} + 2Mar \sin^2 \theta (r^2 + a^2)\Sigma (\partial_r \omega) \right], \quad (16)$$

$$C_2 \equiv \frac{2Ma \sin^2 \theta}{(r^2 + a^2)^2 \Sigma^2} \times \left[-r^6 + a^2(-2 + \cos^2 \theta)r^4 + 4Ma^2 \sin^2 \theta r^3 + a^4(1 - 2 \sin^2 \theta)r^2 + a^6 \cos^2 \theta \right], \quad (17)$$

$$C_3 \equiv (r - M)A + a^2 \sin^2 \theta \times \left[-r^3 - 3Mr^2 + (2M^2 - a^2 \cos^2 \theta)r + a^2 M \cos^2 \theta \right]. \quad (18)$$

It follows that all the four highest-order derivative terms of equation (14) have definite signs; thus, the Biot-Savart law now become an elliptic type in the entire simulation region, because we adopt a physical observer, ZAMO.

The Gauss's law (B31) can also be re-written with respect to αA_t and A_φ . Multiplying $[\Delta/(r^2 + a^2)]^2$ on both sides, we obtain

$$\frac{A}{\Sigma^2} \frac{\partial^2(\alpha A_t)}{\partial r_*^2} + D_1 \frac{\partial(\alpha A_t)}{\partial r_*} - \frac{\Delta A}{(r^2 + a^2)\Sigma^2} (\partial_r \omega) \frac{\partial A_\varphi}{\partial r_*} + \frac{\Delta A \sin^2 \theta}{(r^2 + a^2)^2 \Sigma^2} \frac{\partial^2(\alpha A_t)}{\partial \xi^2}$$

$$+ \frac{2\Delta \cos \theta}{(r^2 + a^2)^2 \Sigma^3} \left[(r^2 + a^2)A - a^2 \Delta \Sigma \sin^2 \theta \right] \frac{\partial(\alpha A_t)}{\partial \xi} + \frac{2\Delta \sin^2 \theta}{(r^2 + a^2)^2 \Sigma^2} \left[-A(\partial_\xi \omega) + \Delta a^2 \cos \theta \cdot \omega \right] \frac{\partial A_\varphi}{\partial \xi} + D_0 A_\varphi = 4\pi\rho \left(\frac{\Delta}{r^2 + a^2} \right)^2, \quad (19)$$

where

$$D_0 \equiv \frac{\Delta A}{(r^2 + a^2)^2 \Sigma^2} \left\{ -\Delta(\partial_r^2 \omega) - \sin^2 \theta (\partial_\xi^2 \omega) + \left[2(r - M) - \Delta \partial_r \left(\ln \frac{\Delta A}{\Sigma} \right) \right] (\partial_r \omega) - \frac{2 \cos \theta}{\Sigma} \left[r^2 + a^2 - \frac{\Delta \Sigma}{A} a^2 \sin^2 \theta \right] (\partial_\xi \omega) \right\} \quad (20)$$

and

$$D_1 \equiv -\frac{A}{(r^2 + a^2)\Sigma^2} \times \left[2(r - M) - \Delta \partial_r \left(\ln \frac{(r^2 + a^2)A}{\Sigma} \right) \right] \quad (21)$$

Note that $\partial^2 A_\varphi / \partial r_*^2$ and $\partial^2 A_\varphi / \partial \xi^2$ terms vanish in equation (19).

2.4. Boundary conditions

We search for the stationary solution that satisfy the Gauss's law (19) and the Biot and Savart law (14). To this end, we must impose boundary conditions αA_t and A_φ , or equivalently on A_t and A_φ . In the present paper, we solve these two equations in the first and fourth quadrants of the poloidal plane (r, θ) . The region is bordered by

- the polar boundary at $\theta = 0$ (north polar axis) and at $\theta = \pi$ (south polar axis),
- the inner boundary at $r = r_H$, and
- the outer boundary at $r = r_{\text{out}}$, where $r_{\text{out}} \gg r_g \equiv GMc^{-2} = M$.

In this subsection, we describe the boundary conditions at these three boundaries.

At the northern and southern polar boundaries, we impose $E_\theta = \partial_\theta A_t = 0$, that is, a Neumann condition on A_t . We also impose

$B^\theta \propto F_{\varphi r} = -\partial_r A_\varphi = 0$. Thus, we put $A_\varphi = 0$ at $\theta = 0$ and π and measure the magnetic flux function A_φ from the rotation axis.

At the inner boundary, we impose $\mathbf{E} \cdot \mathbf{B} = 0$ and $F_{\varphi r} = 0$, where $F^{r\theta} = 0$ is assumed at $t = 0$. For instance, in ZAMO, these conditions constrain that both the radial component of the electric field and the meridional component of the magnetic field vanish at the inner boundary.

At the outer boundary ($r = r_{\text{out}} \gg M$), we impose $\mathbf{E} \cdot \mathbf{B} \propto (\partial_r A_t)(\partial_\theta A_\varphi) - (\partial_\theta A_t)(\partial_r A_\varphi) = 0$ and $\partial_r A_\varphi = 0$, the latter of which comes from the assumption of a split-monopole magnetic field, $J_{\text{eq}}^\varphi \propto r^{-4}$. Thus, in the present paper we impose the Neumann condition, $\partial_r A_t = 0$. However, in general, if we impose the magnetic field direction, $\partial_r A_\varphi / \partial_\theta A_\varphi$ (e.g., if we adopt a paraboloidal magnetic field, see BZ77 for details), $\mathbf{E} \cdot \mathbf{B} = 0$ constrains the direction of the $A_t = \text{constant}$ surface at the outer boundary.

2.5. Disk toroidal current

We assume that the plasmas in an ADAF produce a toroidal current $J_{\text{eq}}^\varphi = C_{\text{eq}} r^{-4}$ near the equator all the way to the horizon within the colatitudes $87^\circ < \theta < 93^\circ$; outside of this equatorial region, $J_{\text{eq}}^\varphi = 0$ is assumed. For a slowly rotating BH, this disk current produces a split-monopole magnetic field (BZ77).

The normalization factor C_{eq} is adjusted so that the meridionally averaged, ZAMO-measured radial magnetic field strength at $r = 2M$,

$$\langle B^r(2M) \rangle \equiv \frac{\int_0^\pi \tilde{B}^r(2M, \theta) \sqrt{A} \sin \theta d\theta}{\int_0^\pi \sqrt{A} \sin \theta d\theta}, \quad (22)$$

may match a fraction of the equipartition field strength (Yuan & Narayan 2014),

$$B_{\text{eq}}(r) = 9.7 \times 10^7 \left(\frac{\dot{m}}{M_1} \right)^{1/2} \left(\frac{r}{2M} \right)^{-5/4} \text{ G}, \quad (23)$$

which is obtained if there is an equipartition between the magnetic field energy density and

the plasma internal energy density; the alpha viscous parameter is assumed to be 0.3. The dimensionless accretion rate \dot{m} is defined by

$$\dot{m} \equiv \frac{\dot{M}}{\dot{M}_{\text{Edd}}}, \quad (24)$$

where \dot{M} denotes the mass accretion rate. The Eddington accretion rate is defined by

$$\dot{M}_{\text{Edd}} \equiv \frac{L_{\text{Edd}}}{\eta_{\text{eff}} c^2} = 1.39 \times 10^{19} M_1 \text{ g s}^{-1}, \quad (25)$$

where L_{Edd} denotes the Eddington luminosity; the conversion efficiency is assumed to be $\eta_{\text{eff}} = 0.1$.

In the present paper, we adopt a relatively small mass accretion rate, $\dot{m} = 2.25 \times 10^{-4}$, and $\langle B^r(2M) \rangle = B_{\text{eq}}(2M)$.

2.6. Stationary solution

In the present paper, we consider a ten solar-mass BH, $M_1 \equiv M/(10M_\odot) = 1$, and solve equations (14) and (19) iteratively in the region $r_{\text{H}} < r \leq 20M$ and $0 \leq \theta \leq \pi$. The solved electromagnetic fields are presented in figure 1. In each panel, thin black curves show the equi- A_φ contours, which indicate the poloidal magnetic field lines for a distant static observer if $a = 0$. We superpose $\mathbf{E} \cdot \mathbf{B} / [B_{\text{eq}}(r = 2M)]^2$, whose values are indicated in the color code. The left and right panels correspond to the cases of $a = 0$ and $a = 0.9M$, respectively.

In the left panel, $\mathbf{E} \cdot \mathbf{B} = 0$ holds everywhere; thus, the background color is entirely white. It follows that the poloidal magnetic field becomes radial for a slowly rotating BH when $J_{\text{eq}}^\varphi \propto r^{-4}$, which is consistent with the analytical conclusion (Blandford & Znajek 1977; McKinney & Narayan 2007). Because of $a = 0$, there exists no magnetic-field-aligned electric field, E_{\parallel} ; thus, A_φ is solved only from the Biot-Savart law.

However, as the BH spins up (i.e., if $a \neq 0$), the right panel shows that there arises a non-vanishing E_{\parallel} due to the relative rotational motion of the magnetic field lines with respect to

the space time. At the same time, equi- A_φ lines deviates from a radial shape, as the solid curves indicate. For a rapidly rotating case, $a = 0.9M$, the magnetic field lines are laterally pushed toward the rotation axis in the ergosphere (Tanabe & Nagataki 2008; Tchekhovskoy et al. 2010). Note that the magnetosphere is assumed to be vacuum in the present analysis, while it is force-free (i.e., plasma-filled) in Blandford & Znajek (1977); Tanabe & Nagataki (2008); Tchekhovskoy et al. (2010). To examine how the magnetic field lines are actually deformed for a physical observer, we adopt ZAMO and plot in figure 2 the radial ($\tilde{B}^{\hat{r}}$, left panel) and the meridional ($\tilde{B}^{\hat{\theta}}$, right panel) components of the magnetic field, where their explicit expressions are given by equations (A12) and (A13). It shows that $|\tilde{B}^{\hat{\theta}}|$ is kept below $|\tilde{B}^{\hat{r}}|$ except for the equatorial region where $\tilde{B}^{\hat{r}}$ vanishes by symmetry. To compare with slowly rotating cases, we adopt the same power-law in the disk current, $J^\varphi_{\text{eq}} \propto r^{-4}$, for all the cases of a . To avoid a substantial $|\tilde{B}^{\hat{\theta}}|$ in the lower-latitude ergosphere, we could adopt another functional form of J^φ_{eq} for $a \neq 0$; however, such a fine-tuning is out of the scope of the present paper.

We assume a positive J^φ_{eq} ; thus, $F_{\theta\varphi}$ (i.e., the radial component of the magnetic field) is positive (or negative) in the northern (or southern) hemisphere. Accordingly, a positive (or a negative) sign of $\mathbf{E} \cdot \mathbf{B}$ indicates that the electric field points outwards in the northern (or southern) hemisphere. Thus, as plasmas are created (via photon-photon collisions) near the horizon, $r < 2M$, electrons (or positrons) are accelerated inwards (or outwards) in both hemispheres in this stationary solution. Such accelerated electrons and positrons produce electric currents in the magnetosphere, whose poloidal components modifies the poloidal electric field through the Ampere's law. In the next section, we will focus on the temporal evolution of the electromagnetic fields and the particle distribu-

tion functions starting from the initial conditions described in this section.

3. THE PARTICLE-IN-CELL (PIC) SCHEME

Let us look briefly at the collisionless nature of the plasmas in § 3.1, before turning to a closer examination of the temporal evolution of the BH magnetosphere in the rest of this section.

3.1. Collisionless plasmas

Denoting the density of a pair plasma with $n_\pm = \kappa n_{\text{GJ}}$, we can express the collision frequency as

$$\nu_c \sim \kappa n_{\text{GJ}} \sigma c, \quad (26)$$

where σ refers to the collisional cross section, and

$$n_{\text{GJ}} \equiv \omega_{\text{H}} B / (4\pi c e) \quad (27)$$

denotes the Goldreich-Julian (GJ) number density, which is rotationally induced; e denotes the charge on the electron. If the plasma density is comparable to the GJ value, κ becomes of the order of unity.

Let us evaluate the cross section by $\sigma \sim \pi l_c^2$, where l_c denotes the typical impact parameter. Equating the potential and kinetic energies, we find $e^2/l_c \sim (\gamma - 1)m_e c^2$. Then combining it with equation (26), we obtain

$$\nu_c \sim \frac{\kappa \pi n_{\text{GJ}} e^4}{\gamma^2 m_e^2 c^3}, \quad (28)$$

where $\gamma \gg 1$ is assumed. On the other hand, the gyro frequency is given by

$$\nu_{\text{B}} = \frac{eB}{2\pi\gamma m_e c}. \quad (29)$$

We thus obtain

$$\frac{\nu_c}{\nu_{\text{B}}} \sim \frac{\pi \kappa a r_0}{4 \gamma M r_{\text{H}}}, \quad (30)$$

where $r_0 \equiv e^2/(m_e c^2)$ denotes the classical electron radius. Since $r_0/r_{\text{H}} \sim 10^{-19} M_1^{-1}$ holds, we can conclude that the collision frequency is

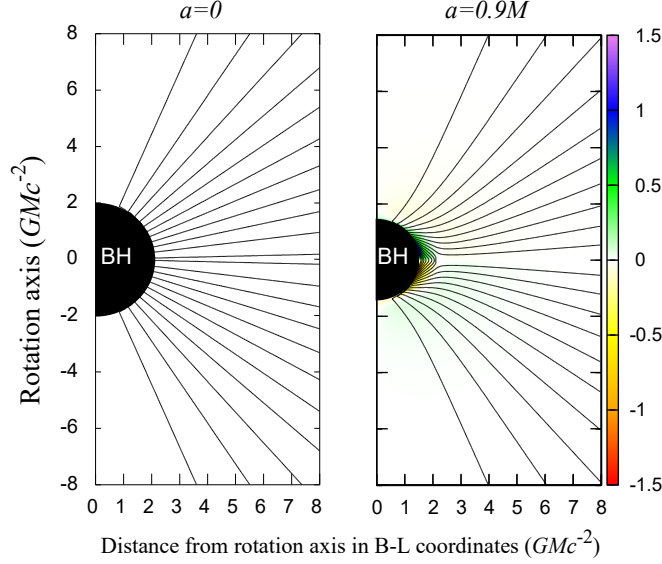


Figure 1. Stationary equi- A_φ contours (solid curves) and the distribution of $\mathbf{E} \cdot \mathbf{B} / B_{\text{eq}} (2M)^2$ (color) on the poloidal plane (r, θ) . The equatorial current density is assumed to depend on r as $J^\varphi_{\text{eq}} \propto r^{-4}$. The ordinate represents the distance along the rotational axis of the BH, while the abscissa does the distance $r \sin \theta$ from the rotation axis. Both axes show the lengths in the Boyer-Lindquist coordinates, normalized by the gravitational radius, $r_g = GMc^{-2} = M$. The equatorial plane corresponds to the ordinate of 0. The black filled circle shows the BH. Left panel shows the equi- A_φ contours when $a = 0$, in which case the solid curves denote the magnetic field lines measured by a distant static observer. For $a = 0$, there arises no electric fields along the magnetic field lines; thus, the background color is entirely white. Right panel shows the case of $a = 0.9M$. The amplitude of $\mathbf{E} \cdot \mathbf{B}$ increases with increasing a , because the frame-dragging effect increases with increasing BH's spin, a .

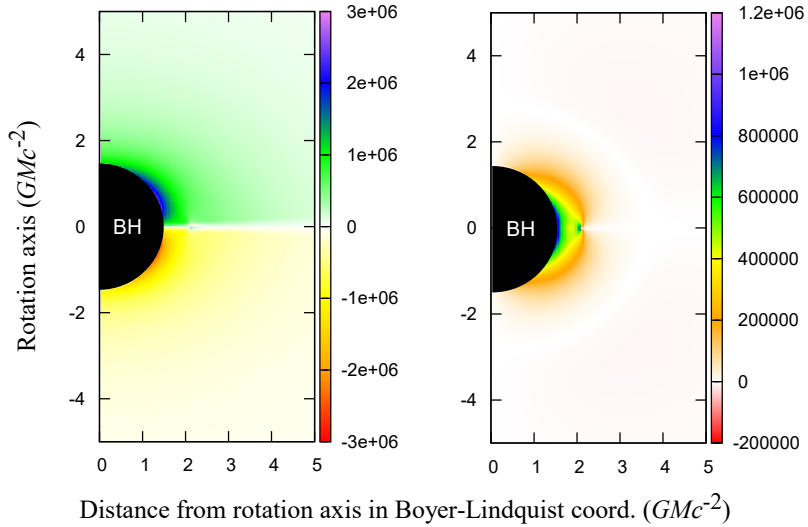


Figure 2. Poloidal magnetic field measured in ZAMO at $t = 0$ for $a = 0.9M$. The abscissa and ordinate are common with figure 1, but the BH vicinity is closed up. Left and right panels show $B^{\hat{r}}(\text{ZAMO})$ and $B^{\hat{\theta}}(\text{ZAMO})$, respectively, in Gauss.

much less than the gyro frequency, and that the assumption of collisionless plasmas in the PIC scheme is justified. This conclusion solely comes from the fact that the GJ density corresponds to a high vacuum in BH or pulsar magnetospheres.

It should be noted that the Ohm's law, which is necessary to close the system of equations in MHD, requires that many collisions should take place within a single gyration. However, equation (30) shows this assumption cannot be justified in a black hole magnetosphere unless the plasma density greatly exceeds the GJ value. In the present paper, we thus construct the electric current from the actual motion of charged particles, adopting the PIC scheme. By this method, we can, for instance, incorporate the currents carried by the drift motion of charged particles, as well as the anisotropic distribution of particles' momenta (e.g., along and perpendicular to the magnetic field lines).

3.2. The Maxwell equations

In the present paper, we assume $F_{\varphi t} = 0$ throughout the simulations. Accordingly, together with $\partial_\varphi = 0$ for all the quantities, we find $\partial_t F_{\theta\varphi} = 0$ and $\partial_t F_{\varphi r} = 0$ from the Faraday's law. Thus, in the present paper, we treat both B^r and B^θ are constant in time (and hence unchanged from the initial condition), and solve the temporal evolution of only F_{rt} , $F_{\theta t}$, and $F^{r\theta}$. This assumption of $F_{\varphi t} = 0$ is justified as long as the toroidal currents carried by the simulated particles are small compared to the stationary, equatorial toroidal current that is carried by the accreting plasmas.

Under this assumption, the Faraday and Ampere's laws give

$$\frac{\partial F^{r\theta}}{\partial t} = -\frac{\Delta}{\Sigma^2} \left(\frac{\partial F_{\theta t}}{\partial r} - \frac{\partial F_{rt}}{\partial \theta} \right), \quad (31)$$

$$\frac{\partial F_{rt}}{\partial t} = \frac{\Sigma^2}{A} \left[\frac{1}{\sqrt{-g}} \frac{\partial}{\partial r} (\sqrt{-g} F^{r\theta}) - 4\pi J^r \right], \quad (32)$$

$$\frac{\partial F_{\theta t}}{\partial t} = \frac{\Sigma^2 \Delta}{A} \left[-\frac{1}{\sqrt{-g}} \frac{\partial}{\partial r} (\sqrt{-g} F^{r\theta}) - 4\pi J^\theta \right]. \quad (33)$$

Replacing the r derivatives with r_* derivatives, and introducing the following dependent variables,

$$\begin{aligned} B &\equiv \sqrt{-g} F^{r\theta}, \\ D &\equiv F_{rt}, \\ E &\equiv F_{\theta t} \sin \theta, \end{aligned} \quad (34)$$

all of which are well-behaved at the horizon, we can rewrite the three Maxwell equations (31)–(33) into

$$\frac{\partial B}{\partial t} = -c_1 \frac{\partial E}{\partial x} + c_2 \frac{\partial D}{\partial y} \quad (35)$$

$$\frac{\partial D}{\partial t} = c_3 \frac{\partial B}{\partial y} - 4\pi \frac{\Sigma^2}{A} J^r \quad (36)$$

$$\frac{\partial E}{\partial t} = -c_4 \frac{\partial B}{\partial x} - 4\pi \frac{\Sigma^2}{A} \Delta \sin \theta \cdot J^\theta \quad (37)$$

where

$$x \equiv r_*, \quad y \equiv 1 - \cos \theta, \quad (38)$$

$$c_1 \equiv \frac{r^2 + a^2}{\Sigma}, \quad c_2 \equiv \frac{\Delta \sin^2 \theta}{\Sigma}, \quad (39)$$

$$c_3 \equiv \frac{\Sigma}{A}, \quad c_4 \equiv \frac{\Sigma(r^2 + a^2)}{A}. \quad (40)$$

All the coefficients c_1 , c_2 , c_3 , and c_4 are positive definite. Both c_1 and c_4 are close to unity in the entire region. However, $c_2 \ll 1$ holds near the horizon or near the pole but $c_2 \rightarrow 1$ at $r \gg M$ in the lower latitudes. We have $c_3 \ll 1$ at $r \gg M$ and $c_3 \approx 0.25$ near the horizon. Note that the singular behaviour (i.e., the polynomial pole) at $\theta = 0$ in equations (32) and (33) is eliminated by introducing a new meridional coordinate, y .

To solve these three Maxwell equations (eqs. [35]–[37]), we must impose appropriate boundary conditions that are consistent with the initial, stationary state (§2.4). Along the northern and southern polar axes (i.e., at $\theta = 0$ and $\theta = \pi$), we impose

$$B = 0, \quad \frac{\partial D}{\partial y} = 0, \quad E = 0. \quad (41)$$

At the inner boundary, $x = r_* = -\infty$, we impose

$$\begin{aligned} \frac{\partial B}{\partial x} = 0, \quad \tilde{E}_{\hat{r}} \propto D + \omega F_{r\varphi} = 0, \\ \frac{\partial E}{\partial x} = \left(\frac{\partial E}{\partial x} \right)_{t=0}, \end{aligned} \quad (42)$$

where the quantity within $()_{t=0}$ indicates the initial value at $t = 0$. At the outer boundary, $x = r_* = r_{\text{out}}$, we impose

$$\frac{\partial B}{\partial x} = 0, \quad D = 0, \quad \frac{\partial E}{\partial x} = \left(\frac{\partial E}{\partial x} \right)_{t=0}. \quad (43)$$

Note that we set $B = 0$ in the entire region at $t = 0$.

3.3. Particle equation of motion

In a highly vacuum BH magnetosphere, charged leptons are decelerated by the radiation-reaction forces. To include these forces from the first principles, we must adopt tiny time steps and consider the force on one part of the charge by the fields of another part, taking account of retardation within the particle itself. However, in actual simulations, it is unrealistic to adopt such tiny timesteps. Thus, as a compromise, we include the radiation reaction force as a friction term in the equation of motion (EOM).

With such a friction term, the EOM can be expressed as (Thorne & MacDonald 1982; Hughes et al. 1994; Bacchini et al. 2018)

$$\begin{aligned} \frac{du_i}{dt} = -\alpha u^t \partial_i \alpha + u_k \partial_i \beta^k - \frac{1}{2} \frac{u_j u_k}{u^t} \partial_i g^{jk} \\ + \frac{q}{m} \left(F_{it} + F_{ij} \frac{u^j}{u^t} \right) + \frac{(F_{\text{rad}})_i}{u^t}, \end{aligned} \quad (44)$$

where α is defined by equation (8), $\beta^r = \beta^\theta = 0$, $\beta^\varphi = g_{t\varphi}/g_{\varphi\varphi}$, q/m refers to the charge-to-mass ratio, and

$$u^t = \frac{\sqrt{1 + g^{jk} u_j u_k}}{\alpha}. \quad (45)$$

The Latin indices run over 1, 2, 3. We can evaluate the radiation-reaction force by the covariant form, (§ 17.8 of Jackson 1962)

$$F_{\text{rad}}^j = \frac{2}{3} \frac{r_0}{c} \left(\frac{d^2 u^j}{d\lambda^2} + u^j \frac{du^\nu}{d\lambda} \frac{du_\nu}{d\lambda} \right), \quad (46)$$

where r_0 denotes the classical electron radius, λ does the particle's proper time, and the Greek indices run over 0, 1, 2, 3. This radiation reaction force includes the effects of any kind of acceleration acting on the particles. For instance, photon emissions as a result of the acceleration in an electro-magnetic field (e.g., via the synchro-curvature process) and that in a gravitational field, are included (Appendix D). However, this radiation-reaction force does not include the effect of inverse-Compton scatterings, which should be considered separately in future works.

Definition of the four velocity u^μ gives

$$\frac{dr}{dt} = \frac{u^r}{u^t}, \quad (47)$$

$$\frac{d\theta}{dt} = \frac{u^\theta}{u^t}, \quad (48)$$

and

$$\frac{d\varphi}{dt} = \frac{u^\varphi}{u^t}. \quad (49)$$

For presentation purpose, we can convert $u_i = dx_i/d\lambda$ in terms of the ZAMO-measured spatial velocity, $u_{\hat{j}}$, as described in Appendix A.

We integrate both equations (44) and (47)–(49) in the phase space with the global time variable t , which corresponds to the proper time of a distant static observer (i.e., us).

Let us briefly describe the boundary conditions on the motion of electrons and positrons. Due to the symmetry, we assume that the particles moving across the polar axis (at $\theta = 0$ or π) will be reflected equator-ward with opposite meridional velocity. Both the inner and outer boundaries are treated as particle sinks. Thus, when particles move across these two radial boundaries, they are excluded from the simulation.

3.4. Plasma supply

In BH magnetospheres, pairs can be supplied via two-photon and/or one-photon (i.e., magnetic) pair production processes. In the present paper, we focus on the former process, and consider the collisions of MeV photons emitted from the equatorial ADAF via Bremsstrahlung. In subsequent papers, we will also consider the collisions between the gap-emitted (inverse-Compton) photons and the ADAF-emitted (synchrotron) photons.

The pair supply rate (pairs per second per volume) is given by

$$\dot{N}_{\pm} = c\sigma_{\gamma\gamma}n_{\gamma}^2, \quad (50)$$

where $\sigma_{\gamma\gamma}$ denotes the total cross section of photon-photon pair production, and n_{γ} does the MeV photon density. Adopting the Newtonian self-similar ADAF model (Mahadevan 1997), and assuming that the most energetic MeV photons are emitted within $r = 4M$, we obtain (Appendix C)

$$\dot{N}_{\pm} \approx 1.0 \times 10^{24} \dot{m}^4 M_1^{-2} \max \left[\left(\frac{r}{4M} \right)^{-4}, 1 \right] \quad (51)$$

in cgs unit (i.e., in pairs $\text{s}^{-1} \text{cm}^{-3}$).

We randomly introduce a macro particle in each cell at every time step with probability $1/k_{\text{create}} = 0.1$; that is, particles are injected in each cell at every $k_{\text{create}} = 10$ time steps on average. In this case, each created macro positron or electron has the electric charge

$$q_i = \pm e \dot{N}_{\pm} k_{\text{create}} \Delta_t \Delta_V, \quad (52)$$

where Δ_t denotes the interval of each time step, and Δ_V the invariant volume of each cell. Note that $\Delta_t \Delta_V = \sqrt{-g} dt dr d\theta d\varphi = 2\pi \sqrt{-g} \Delta_t \Delta_r \Delta_{\theta}$ holds, where Δ_r and Δ_{θ} denote the intervals in Boyer-Linquist radial and meridional coordinates, both of which are non-uniformly gridded.

In the initial state, there are no macro particles in any cell. As the PIC simulation proceeds, the number of macro particles increases

with t to saturate at a few hundred in each PIC cell on average. Here, the maximum value of the Courant number is set to be 0.5 for uniform grid intervals in $x = r_*$ and $y = 1 - \cos\theta$ coordinates. In total, there are about 3×10^8 macro particles in the entire simulation region.

3.5. Nonstationary magnetosphere

It is checked *a posteriori* (§ 4.2) that the invariant grid intervals resolve the skin depth

$$l_p = \frac{c}{\omega_p}, \quad (53)$$

at every point at any elapsed time, where the plasma frequency ω_p is computed by the plasma density n_{\pm} and its mean Lorentz factor $\langle\gamma\rangle$ as

$$\omega_p = \sqrt{\frac{4\pi e^2 n_{\pm}}{m_e \langle\gamma\rangle}}. \quad (54)$$

For stellar-mass BHs, we obtain

$$\frac{l_p}{r_g} = 6.84 \times 10^{-2} k \gamma_6^{1/2} \left(\frac{a}{M} \cdot \frac{B}{B_{\text{eq}}} \right)^{-1/2} M_1^{-1/4}, \quad (55)$$

where $\gamma_6 \equiv \langle\gamma\rangle/10^6$, and

$$k \equiv \kappa^{-1/2} \dot{m}^{-1/4} \left(\frac{r}{r_H} \right)^{5/8} \left(\frac{m_e}{m_p/1836} \right)^{1/2}; \quad (56)$$

m_p denotes the rest mass of the proton.

To resolve the skin depth, l_p , most PIC simulations are performed in one or two dimensions with small ion-to-electron mass ratios (e.g., Bohdan et al. (2019)), covering limited time and length scales. In the present paper, adopting a heavy electron mass of $m_e = m_p/20$, we perform a two-dimensional PIC simulation within about ten gravitational radii over the time duration of several hundred dynamical time scales. We rescale every expression according to this modified electron mass. Under this assumption of heavy charged leptons, we need about 10^3 grid points to fully resolve the skin depth.

On these grounds, we adopt a radial grid of 960 uniform cells between $-15.81807 < x < 12.82443$, which corresponds to $1.46514M < r < 13.68548M$, and 1920 uniform cells between $0 < y = 1 - \cos\theta < 2$, which corresponds to $0^\circ < \theta < 180^\circ$. We present the explicit expression of the discretized Maxwell equations and the particle equation of motion in Appendix E. To construct the electric currents from particle motion (Appendix F), we adopt the area weighting (Villasenor & Buneman 1992).

3.5.1. Electromagnetic fields

We start with the magnetic-field-aligned electric field. In figure 3, we present the distribution of $\mathbf{E} \cdot \mathbf{B}/[B_{\text{eq}}(2M)]^2$. For $M = 10M_\odot$ and $\dot{m} = 2.25 \times 10^{-4}$, we obtain $B_{\text{eq}}(2M) = 1.452 \times 10^6$ G. The left and right panels show the distribution of $\mathbf{E} \cdot \mathbf{B}/[B_{\text{eq}}(2M)]^2$ at $t = 0$ and $t = 430M$, respectively. In the northern hemisphere, since $F_{\theta\varphi} > 0$ holds, a positive (or a negative) sign of $\mathbf{E} \cdot \mathbf{B}$ indicates that an outward (or an inward) electric field arises along the local magnetic field lines. In the same manner, in the southern hemisphere, it follows from $F_{\theta\varphi} < 0$ that a positive (or negative) sign of $\mathbf{E} \cdot \mathbf{B}$ means an inward (or an outward) electric field.

At $t = 0$, there are no poloidal currents in the magnetosphere because of the lack of plasmas. Thus, the magnetic field has no toroidal component. Accordingly, the rotational energy of the BH is not being extracted. On the other hand, because of the relative motion of the magnetic field lines with respect to the space time, there appears a strong electromagnetic field along the magnetic field line. The left panel of figure 3 shows that such a magnetic-field-aligned electric field is exerted in both hemispheres.

As time elapses, $|\mathbf{E} \cdot \mathbf{B}|$ evolves, exerting electric currents in the magnetosphere. These currents modify the poloidal electric field through the Ampere's law. For example, at $t = 430M$ in the northern hemisphere, the right panel shows that a negative $\mathbf{E} \cdot \mathbf{B}$ appears in the

higher-middle latitudes, exerting inwards currents there. In the same manner, in the southern hemisphere, \mathbf{E} points inwards in the higher-middle latitudes outside the ergosphere. Note that $F_{\theta\varphi}$ changes sign across the equator.

Because of this nearly symmetric distribution of the electric field between the two hemispheres, electrons (or positrons) are accelerated outwards (or inwards) in the higher-middle latitudes in both hemispheres. In the lower latitudes, however, positrons (or electrons) are accelerated outwards (or inwards) by the strong magnetic-field-aligned electric field in both hemispheres. As a result, currents flow inwards in the middle latitudes and flow outwards in the lower latitudes. For the details of the electric currents, see § 3.5.2. Such a pattern of the magnetospheric currents lead to a positive toroidal magnetic field ($\propto F^{r\theta}$) in the northern hemisphere, while a negative $F^{r\theta}$ in the southern hemisphere. Thus, $F^{r\theta}$ vanishes on the equator.

Now let us consider the Poynting flux, or equivalently the BZ flux,

$$T_{\text{em}}{}^r{}_t = \frac{c}{4\pi} F^{r\mu} F_{\mu t} \propto F^{r\theta} F_{\theta t} \quad (57)$$

in the BH vicinity. If it becomes positive, it means that the BH's rotational energy is being extracted electromagnetically. In figure 4, we plot the temporal evolution of $T_{\text{em}}{}^r{}_t(t, r, \theta)$ at $r = r_{\text{H}} + 0.25M$ at four discrete colatitudes as labeled. The ordinate is normalized by the typical BZ flux, which is analytically given by $F_{\text{analytical}} \equiv L_{\text{BZ}}/S_{\text{area}}$, where $S_{\text{area}} \equiv \int \int \sqrt{A} \sin\theta d\theta d\phi$. The BZ power (i.e., the spin-down luminosity) can be estimated to be

$$L_{\text{BZ}} = \frac{1}{128} \left(\frac{a}{M}\right)^2 B_\perp^2 r_{\text{H}}^2 c \quad (58)$$

in the slow-rotating limit, $|a| \ll M$, where B_\perp denotes the averaged strength of the radial magnetic field. It follows from the figure that the solution exhibits rapid plasma oscillations, as

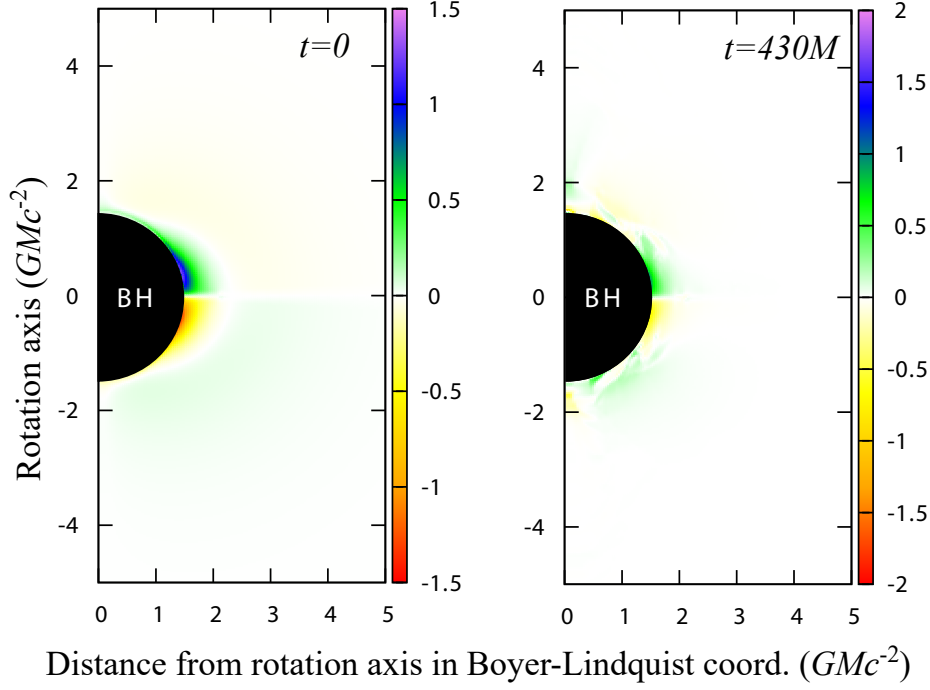


Figure 3. Distribution of $\mathbf{E} \cdot \mathbf{B} / B_{\text{eq}}(2M)^2$ on the poloidal plane (r, θ) for $a = 0.9M$, $B = B_{\text{eq}}$, and $\dot{m} = 2.25 \times 10^{-4}$. Left and right panels show the distribution at $t = 0.00$ and $t = 430.00GMc^{-3}$, respectively. The abscissa and ordinate are common with figure 2. Magnetic surfaces (i.e., constant A_φ lines) are not depicted, but are common with the right panel of figure 1

reported by Levinson & Cerutti (2018). It also follows that the simulated BZ flux is consistent with its analytical estimate. See the supplementary material of Crinquand et al. (2020) for a consistent discussion between the simulated BZ flux and their analytical estimates.

It should be noted that the BZ flux increases during the elapsed time $320M < t < 450M$ along the middle latitudes, $45^\circ \leq \theta \leq 75^\circ$. During this flux-enhancement phase, the BZ flux (i.e., the Poynting flux) fluctuates relatively mildly compared to its amplitude within $45^\circ \leq \theta \leq 60^\circ$. In the present magnetically dominated magnetosphere, in which the magnetic energy density dominates the particles' rest-mass energy densities, particles' energy flux is typically less than 10^{-7} compared to the Poynting flux; thus, we neglect their contribution when we consider the energy flux.

In figure 5, we present the angular dependence of the BZ flux at four elapsed time as labeled.

During the flux-enhancement phase, the BH's rotational energy is efficiently extracted from the middle latitudes, $40^\circ < \theta < 75^\circ$ in the northern hemisphere, and $105^\circ > \theta > 135^\circ$ in the southern hemisphere.

To smear out the variation, we take a moving average with a period of $5GMc^{-3}$, and plot the BZ fluxes in figure 6. In this particular figure, we compare the results for three accretion rates: the top, middle, and bottom panels show the BZ fluxes at $\dot{m} = 0.000250$, 0.000225 , and 0.000200 , respectively. We find that the flux is enhanced for typically $140 \sim 180$ dynamical time scales, and that the flux peaks in the middle latitudes during the enhancement irrespective of the accretion rate, as the blue dashed ($\theta = 50^\circ$), the blue solid ($\theta = 60^\circ$), and the black dashed ($\theta = 70^\circ$) curves indicate in each panel. For example, at $\theta = 60^\circ$, the FWHMs of the moving-averaged flux become $157M$ and $149M$ in the northern and

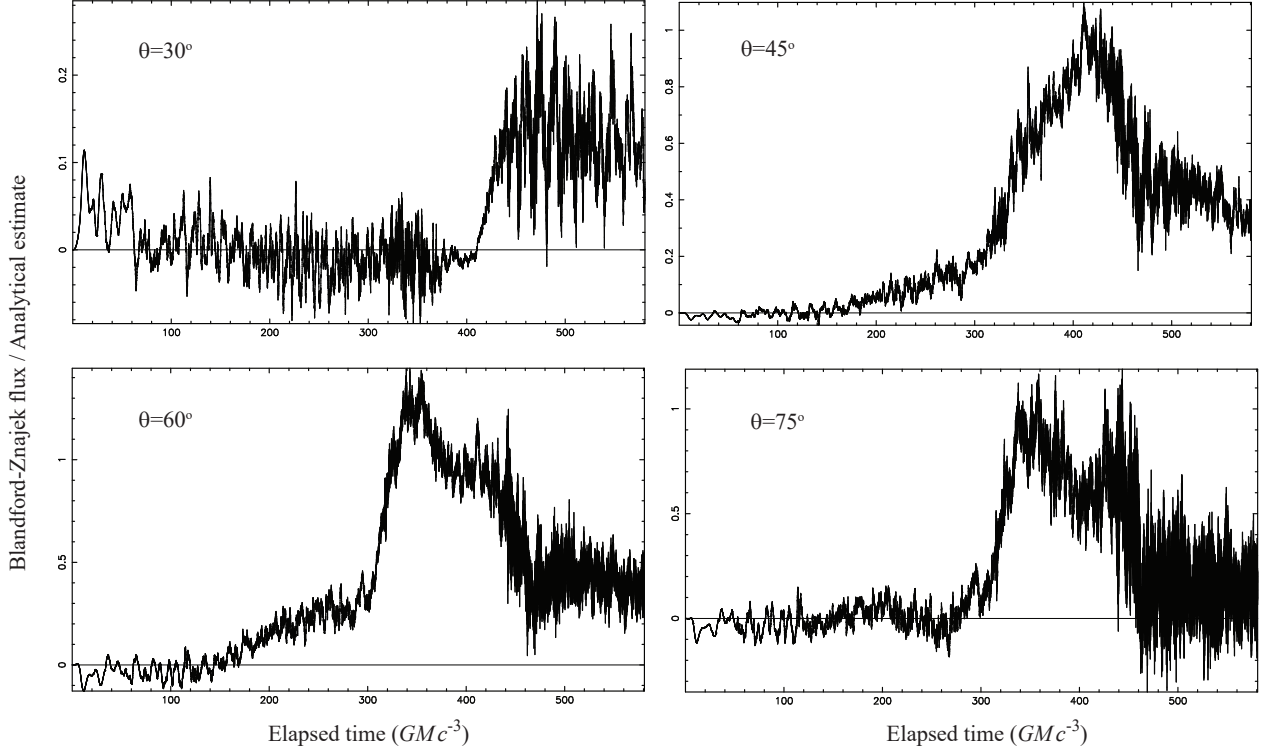


Figure 4. Radial component of the Blandford-Znajek (BZ) flux as a function of the elapsed time at radius $r = r_H + 0.25M$. The ordinate is normalized by its analytical estimate (see text for details), while the abscissa by the dynamical time scale. Each panel shows the BZ flux at discrete colatitudes as labeled.

southern hemispheres, respectively, when $\dot{m} = 2.50 \times 10^{-4}$ (as the top two panels show). They become $136M$ (northern) and $184M$ (southern) when $\dot{m} = 2.25 \times 10^{-4}$ (middle two panels), and $141M$ (northern) when $\dot{m} = 2.00 \times 10^{-4}$ (bottom left panel). However, it is still not possible to measure the FWHM for the southern hemisphere when $\dot{m} = 2.00 \times 10^{-4}$ (bottom right panel). The flux distributes more symmetrically between northern and southern hemispheres, as the accretion rate increases.

3.5.2. Particle distribution and currents

We next consider the distribution functions of e^\pm 's, and the resultant current distribution. Figure 7 shows the densities of electrons (left) and positrons (middle) at the burst peak, $t = 430M$, in log scale. The right panel shows the GJ value at each point. It follows that both elec-

trons and positrons have greater densities than the GJ value particularly in the lower latitudes. In the polar regions, because of the polarization drift caused by the varying meridional electric field (and the constant radial magnetic field), electrons migrate meridionally to accumulate in $\theta < 15^\circ$ and $\theta > 165^\circ$, whereas positrons in $15^\circ < \theta < 20^\circ$ and $165^\circ > \theta > 160^\circ$ at $t \sim 430M$. In the lower latitudes, the leptonic densities attain $10^{7.7} \text{cm}^{-3}$.

The charged leptons carry electric currents, as depicted in figure 8. In the left and right panels, we present the radial and meridional components of the electric currents at each point in the ZAMO frame. For a quantity $f(r, \theta)$, we plot

$$F = \text{sign} \{ \lg [\max(|f|, 1)], f \}, \quad (59)$$

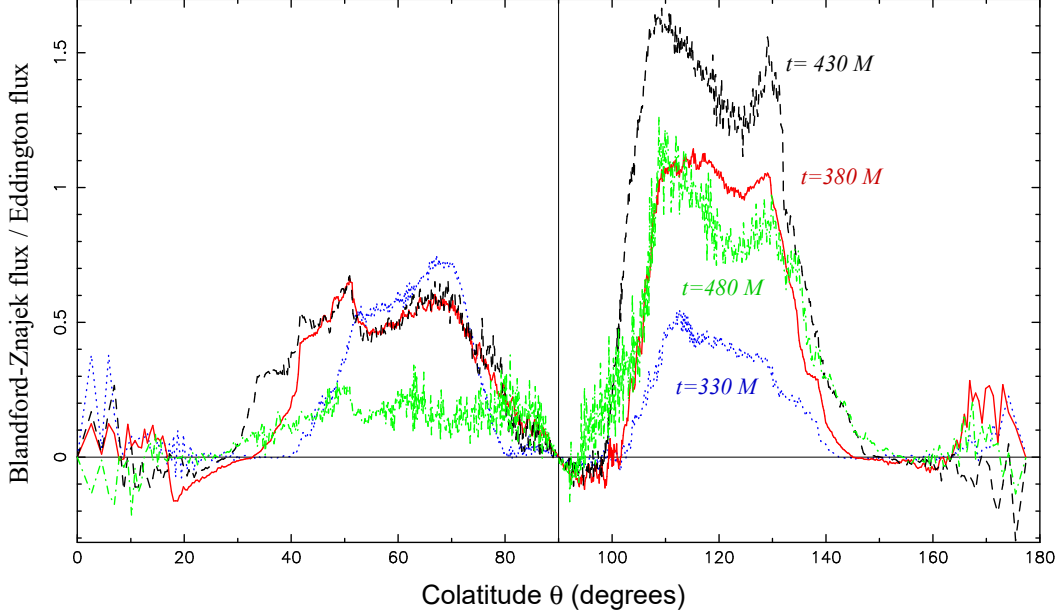


Figure 5. Radial component of the Blandford-Znajek flux as a function of the colatitude angle, θ . The blue dotted, red solid, black dashed, and green dash-dotted curves show the BZ flux at time $t = 330.00GMc^{-3}$, $380.00GMc^{-3}$, $430.00GMc^{-3}$, and $480.00GMc^{-3}$, respectively.

where $\text{sign}(a, b) = |a|$ if $b \geq 0$ and $= -|a|$ if $b < 0$; we set $f = J^{\hat{r}}$ and $J^{\hat{\theta}}$ for the left and right panels, respectively. In the left panel, the yellow-red regions show that currents flow inwards in the middle latitudes, while the blue-violet regions show that they flow outwards in the lower latitudes. These radial currents are closed by meridional currents flowing within the ergosphere, as the right panel shows. For example, in the right panel, the blue (or red) region in the lower-middle latitudes within $r < 2M$ in the northern (or southern) hemisphere shows equator-ward meridional currents. Because of this current closure, it is confirmed that the BZ process is, indeed, facilitated.

To grasp the current distribution more easily, we plot the direction and strength of the poloidal currents as red arrows in figure 9. The current density is averaged over the area in which we compute the direction and length of each arrow. In the figure, the length of the arrows indicates the strength of the current density in logarithmic scale, as indicated by the

right panel. We can confirm the current pattern discussed in the foregoing paragraph. It also follows that the averaged currents mostly flow in the middle and lower latitudes; thus, the low density regions in the polar funnels do not essentially affect the entire structure of the magnetosphere. In this figure, we also plot the charge density, $(n_+ - n_-)/n_{\text{GJ}}$, in color, where n_+ and n_- refer to the positronic and electronic number densities. Values are plotted using the same method as figure 8 (eq. [59]). It follows that the real charge density becomes even greater than the GJ value (right panel of fig. 7), which indicates that the electron-positron plasmas become highly non-neutral near the BH.

We next consider the distribution functions of the charged leptons. The dimensionless distribution functions of e^{\pm} 's, n_{\pm} , are sliced between the colatitude $\theta_1 < \theta < \theta_2$,

$$N_{\pm}(r_*, \gamma) \equiv \frac{1}{n_{\text{GJ}}} \int_{\theta_1}^{\theta_2} d\theta \frac{\partial^2 n_{\pm}(r_*, \theta, \gamma)}{\partial \theta \partial \gamma}. \quad (60)$$

In figure 10, we present N_- and N_+ as a function of r_* and γ (i.e., the Lorentz factor) in the

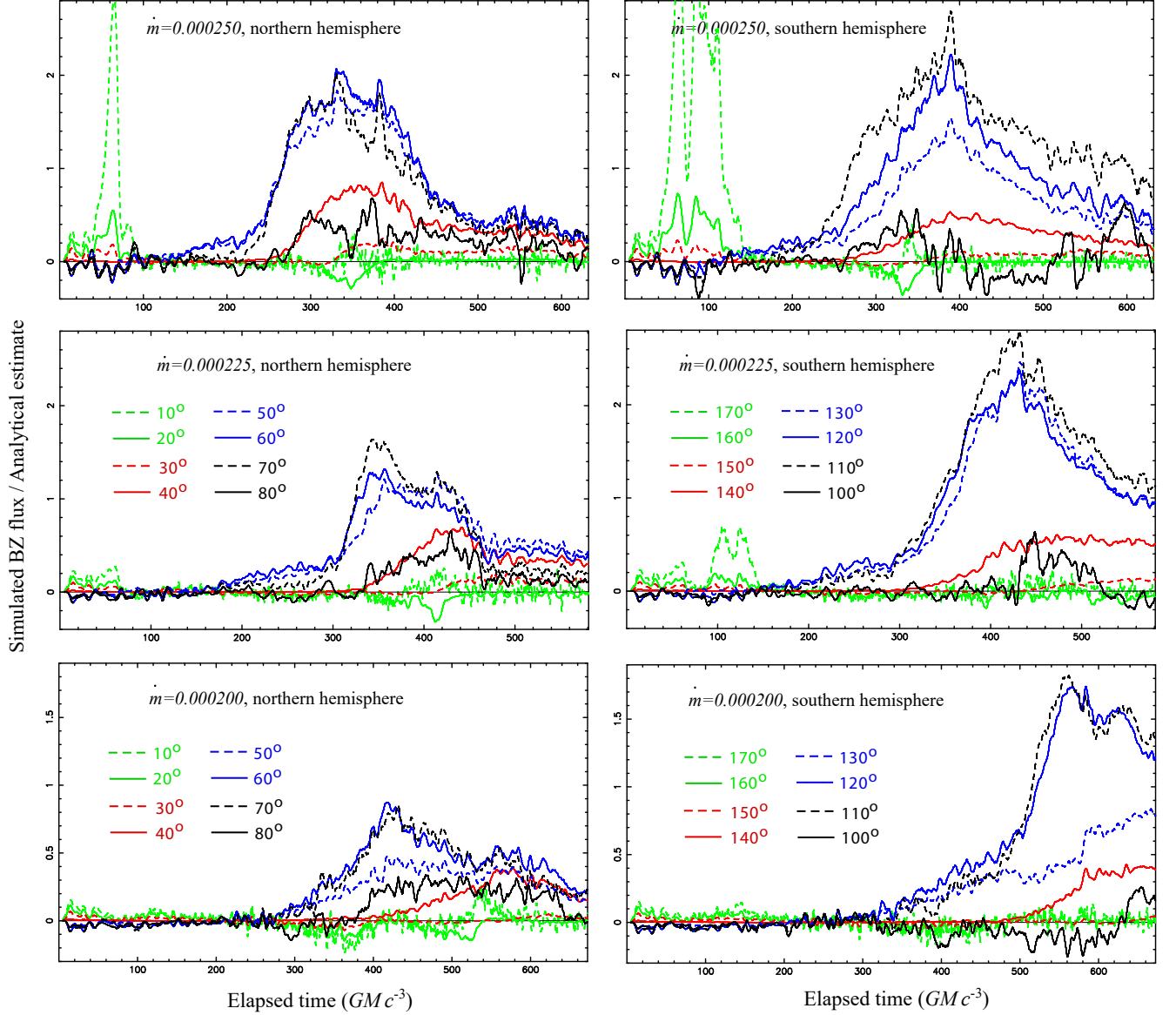


Figure 6. Moving-averaged BZ fluxes with a period of $5GMc^{-3} = 5M$, for three dimensionless accretion rates, $\dot{m} = 2.50 \times 10^{-4}$ (top), $\dot{m} = 2.25 \times 10^{-4}$ (middle), and $\dot{m} = 2.00 \times 10^{-4}$ (bottom). Left (or right) panels depict the BZ flux in the northern (or southern) hemispheres. Each curve denotes the BZ flux at colatitude θ as labeled.

left and right columns, respectively. The range of $\theta \in [\theta_1, \theta_2]$ increases from upper to lower rows as described in the caption. It shows that the Lorentz factors are saturated at a terminal value at each point. The terminal value is determined by the balance between the electrostatic acceleration and the synchro-curvature radiation drag force. Since $|\mathbf{E} \cdot \mathbf{B}|$ increases with decreasing radius significantly at $r_* < 0$ (or equivalently,

at $r < 4.1M$), particles gain large kinetic energies inside $r < 4M$. Nevertheless, by virtue of the residual magnetic-field-aligned electric field, particle motion is kept relativistic in the entire region. Lorentz factors attain $\gamma > 10^{4.5}$ in $r_* < 1M$ (or equivalently, in $r < 4.7M$).

To examine the pitch-angle dependence, in figure 11, we plot $N_{\pm}(r_*, \chi)$, where the pitch angle χ becomes $+1$ (or -1) when a particle is moving

outwards (or inwards) with a very small trans-magnetic-field momentum, and becomes 0 when it has no longitudinal momentum. At $r_* > 0$, particles have small trans-magnetic-field momenta. However, in the higher-middle latitudes, $\theta \sim 40^\circ$, the middle two panels show that electrons (or positrons) migrate outwards with positive $\cos \chi$ (or inwards with negative $\cos \chi$), indicating an inward poloidal current there. Figures 10 and 11 show that particles are highly relativistic with non-thermal and anisotropic distribution functions.

4. DISCUSSION

To sum up, we simulated the evolution of a BH magnetosphere by a PIC scheme, when a poloidal magnetic field is sustained by a disk toroidal current, and when the electron-positron pair plasmas are steadily supplied homogeneously per invariant volume basis. Provided that the mass accretion rate is much less than the Eddington rate, both the electromagnetic fields and the particle distribution functions exhibit rapid variability. The rotational energy of the BH is, indeed, extracted via the Blandford-Znajek process, whose energy flux concentrates in the middle latitudes, particularly during the flux-enhancement phase that lasts approximately 160 ± 20 dynamical time scales. We have demonstrated that the collision time scale is much longer than the gyration time scale (i.e., the Ohm's law cannot be justified), that the pair plasma is highly non-neutral, that the particles' energy distribution is non-Maxwellian, and that the momentum distribution is anisotropic. Thus, we must discard the MHD approximation when we consider the jet launching region around the BH whose mass accretion rate is highly sub-Eddington.

In this section, we discuss the dominant radiative process in § 4.1, the validity of gridding in § 4.2, comparison with other works in § 4.3, and an implication to the collimation of VLBI jets in § 4.4.

4.1. Dominant radiative process

Although the synchro-curvature radiation process is incorporated in the radiative reaction force, F_{rad}^j , ICS are not considered as a radiation drag. Thus, we have to confirm that the ICS process is negligible compared with the synchro-curvature process around stellar-mass BHs accreting at $\dot{m} \ll 1$. Here we briefly compare the pure curvature, pure synchrotron, and ICS processes, and discuss the dominant process. To make a general discussion, we adopt the actual electron mass $m_e = m_p/1836$, instead of $m_p/20$, in this subsection.

The magnitude of the radiation drag force due to the pure curvature process is given by

$$F_{\text{curv}} = \frac{2}{3} e^2 \frac{\gamma^4}{\rho_c^2} = 1.70 \times 10^{-4} \left(\frac{\rho_c}{2M} \right)^{-2} M_1^{-2} \gamma_7^4 \text{ dyn}, \quad (61)$$

where ρ_c refers to the curvature radius of the particle's center of gyration, $2M = 2MGc^{-2}$ the Schwarzschild radius, and $\gamma_n \equiv \gamma/10^n$. If this force balances with the electrostatic force,

$$eE_{\parallel} = 4.80 \times 10^{-5} |E_{\parallel,5}| \text{ dyn}, \quad (62)$$

we find that the particles saturate at the Lorentz factor,

$$\gamma_{\text{curv}} = 7.28 \times 10^6 \left(\frac{\rho_c}{2M} \right)^{1/2} M_1^{1/2} E_{\parallel,5}^{1/4}, \quad (63)$$

where $E_{\parallel,5} \equiv E_{\parallel}/(10^5 \text{ statvolt cm}^{-1})$.

The magnitude of the radiation-drag force due to the pure synchrotron process is given by

$$F_{\text{sync}} = \frac{2}{3} r_0^2 \gamma^2 B^2 \sin^2 \chi = 5.29 \times 10^{-5} \gamma_5^2 B_6^2 \frac{\sin^2 \chi}{0.1} \text{ dyn}, \quad (64)$$

where r_0 denotes the classical electron radius, and χ the pitch angle. Equating equations (62) and (64), we obtain the terminal Lorentz factor

$$\gamma_{\text{sync}} = 9.52 \times 10^4 B_6^{-1} \left(\frac{\sin^2 \chi}{0.1} \right)^{-1/2} E_{\parallel,5}^{1/2}. \quad (65)$$

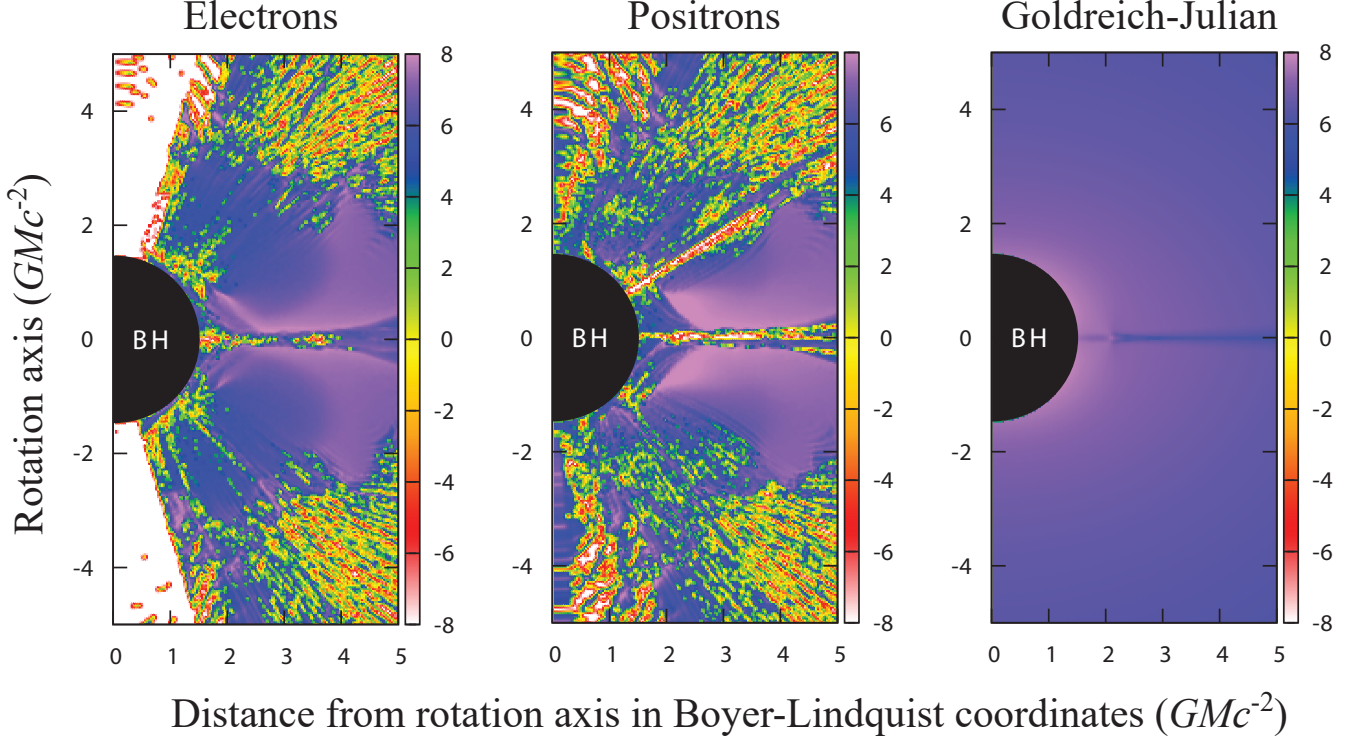


Figure 7. Densities of electrons (left) and positrons (middle), and the Goldreich-Julian density (right), n_{GJ} , in cm^{-3} unit at $t = 430M$. Values are plotted in decadic logarithm. The abscissa and ordinate are common with figure 2.

If $\gamma_{\text{sync}} < \gamma_{\text{curv}}$, the pure synchrotron process dominates the pure curvature process. If $m_e = m_p/1836$, We find that the condition $\gamma_{\text{sync}} < \gamma_{\text{curv}}$ is satisfied, because

$$B_6 \left(\frac{\sin \chi}{0.1} \right) E_{\parallel,5}^{-1/4} \left(\frac{\rho_c}{2M} \right)^{1/2} > 1 \quad (66)$$

is satisfied by the vast majority of the particles. In another word, the synchro-curvature process reduces to the pure synchrotron process for most of the particles. However, since we assume heavy electrons in this paper, the increased gyro radius makes the synchrotron process less efficient; thus, the radiation drag force is given by the synchro-curvature process in general for heavy electrons.

We next compare the pure synchrotron process with the ICS. At radius r from the central BH, the number density of the ADAF

synchrotron photons are given by (Mahadevan 1997)

$$N_{\text{ph}} = \frac{L_{\text{sync}}}{4\pi r^2 h\nu c}, \quad (67)$$

where $h\nu$ refers to the energy of the photons emitted from the ADAF via the synchrotron process. The synchrotron luminosity is given by

$$L_{\text{sync}} = 1.67 \times 10^{36} M_1^{1/2} \dot{m}^{3/2} \text{ ergs s}^{-1}. \quad (68)$$

The typical photon energy is given by equation (22) of Mahadevan (1997). Accordingly, we obtain

$$N_{\text{ph}} = 1.55 \times 10^{20} T_{e,9}^5 M_1 \dot{m} \text{ photons cm}^{-3}, \quad (69)$$

where $T_{e,9}$ refers to the electron temperature, T_e , normalized by $10^9 K$. The ICS drag force per electron (or positron) is given by

$$F_{\text{ICS}} \approx N_{\text{ph}} \sigma_{\text{KN}} \gamma m_e c^2, \quad (70)$$

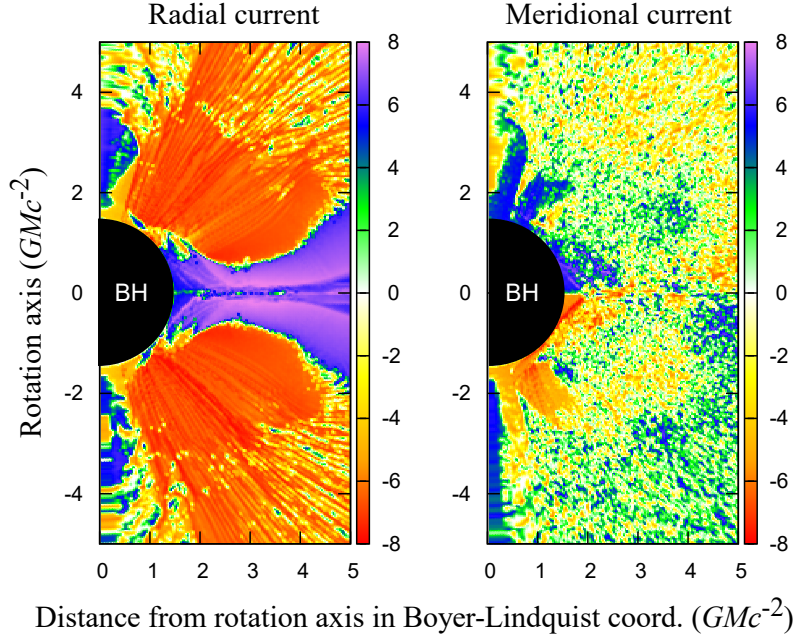


Figure 8. Electric currents measured by ZAMO in the poloidal plane at $t = 430M$. The abscissa and ordinate are common with figure 2. The left panel shows the radial component, $J^{\hat{r}}$, while the right one does the meridional component, $J^{\hat{\theta}}$. To plot the values, we take the decadic logarithm of the absolute value of a quantity, then put the same sign as the quantity. For example, in the left panel, the value of 10^6 (or -10^6) corresponds to an outward (or an inward) current density whose absolute value is 10^6 statampere cm^{-2} . In the same way, in the the right panel, a positive (or a negative) $J^{\hat{\theta}}$ means an equator-ward current in the northern (or southern) hemisphere.

where

$$\sigma_{\text{KN}} \approx \frac{3}{8} \sigma_{\text{T}} x^{-1} \left(\ln 2x + \frac{1}{2} \right), \quad (71)$$

refers to the Klein-Nishina cross section, and $x \approx \gamma$ holds on average. We thus have

$$F_{\text{ICS}} \approx 3.89 \times 10^{-10} M_1 \dot{m} T_{e,9}^5 \quad (72)$$

We thus obtain

$$\gamma_5^2 B_6^2 \left(\frac{\sin \chi}{0.1} \right)^2 M_1^{-1} \dot{m}^{-1} T_{e,9}^{-5} \gg 10^{-5} \quad (73)$$

On these grounds, we obtain $F_{\text{sync}} \gg F_{\text{curv}} \gg F_{\text{ICS}}$ for the actual electron mass. Note that the Lorentz factor will increase with decreasing electron mass. However, for heavy electrons, energy transfer efficiency increases due to their greater mass ratio to protons. Thus, ICS may not be negligible even for stellar-mass BHs. However,

we neglected ICS in this paper, considering future extension to smaller electron masses.

In short, for the actual electron mass, it is possible that the ICS process is negligible compared to the synchro-curvature process, when we consider stellar-mass BHs in a quiescent state. However, for supermassive BHs, we generally obtain $F_{\text{ICS}} > F_{\text{curv}} \gg F_{\text{sync}}$ because of the large curvature radius and the weak magnetic field strength (Hirotani et al. 2016) for the actual electron mass.

4.2. Grid interval versus skin depth

Let us compare the invariant grid interval $\epsilon_{\text{g}} \equiv \Delta_{\text{s}} \equiv \max(\sqrt{g_{rr}}\Delta_r, \sqrt{g_{\theta\theta}}\Delta_{\theta})$ with the skin depth, l_{p} (eq. 53), where Δ_r and Δ_{θ} denote the interval in r and θ coordinates, respectively. Representative values of the dimensionless function $\epsilon(r, \theta)$ are presented in table 1. Because of a constant $\sin \theta \Delta_{\theta}$ gridding, Δ_{θ} increases with de-

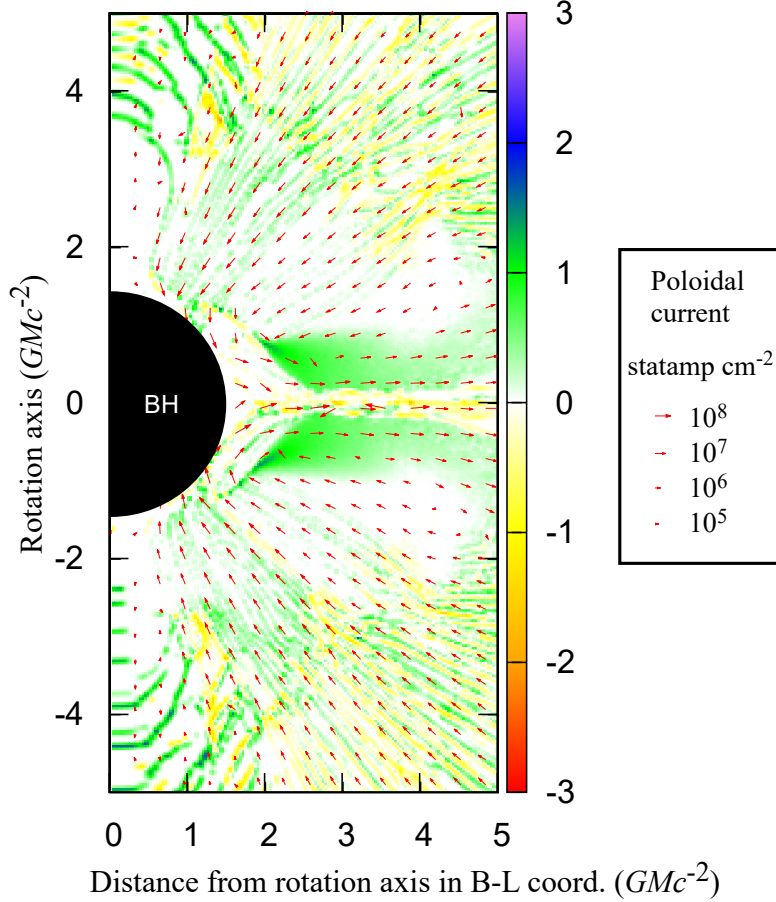


Figure 9. Dimensionless charge density $(n_+ - n_-)/n_{\text{GJ}}$ (color image) and poloidal electric current (red arrows). The abscissa and ordinate are common with figure 2. The charge density is plotted in linear scale. The green (or yellow) regions show positive (or negative) dimensionless charge densities. The right panel shows four example arrow lengths corresponding to the indicated strengths of the poloidal current densities in statampere cm^{-2} .

creasing $\sin \theta$. Note that the dimensionless grid interval ϵ is defined independently from the BH mass.

Adopting heavy electrons, $m_e = m_p/20$, and normalizing the skin depth with r_g , we obtain

$$\frac{l_p}{r_g} = 3.4 (\gamma_5 n_5^{-1})^{1/2} \quad (74)$$

where $\gamma_\nu \equiv \langle \gamma \rangle / 10^\nu$ and $n_\nu \equiv n_\pm / 10^\nu$; $\langle \gamma \rangle$ denotes the averaged Lorentz factor. The highest density region appears in the lower latitudes at $r < 4M$, i.e., at $r_* < -0.25M$. In this region, $n < 10^{7.7} \text{ cm}^{-3}$ and $\langle \gamma \rangle > 10^{4.7}$; thus, we obtain $l_p > 0.108 r_g > 5\Delta_s$ there. Other regions have greater skin depth. Accordingly, the skin depth

can be resolved at every point (and in fact at every time step) during the PIC simulation, although it is marginal when $l_p \sim 5\Delta_s$ happens at the flux peak.

Table 1

Invariant grid interval, $\epsilon(r, \theta) = \Delta_s / r_g$				
r/r_g	$\theta = 2.62^\circ$	29.0°	60.0°	90.0°
8.507	.2762	.0262	.0261	.0260
4.099	.1355	.0217	.0215	.0214
2.021	.0714	.0122	.0117	.0114
1.471	.0557	.0036	.0028	.0026

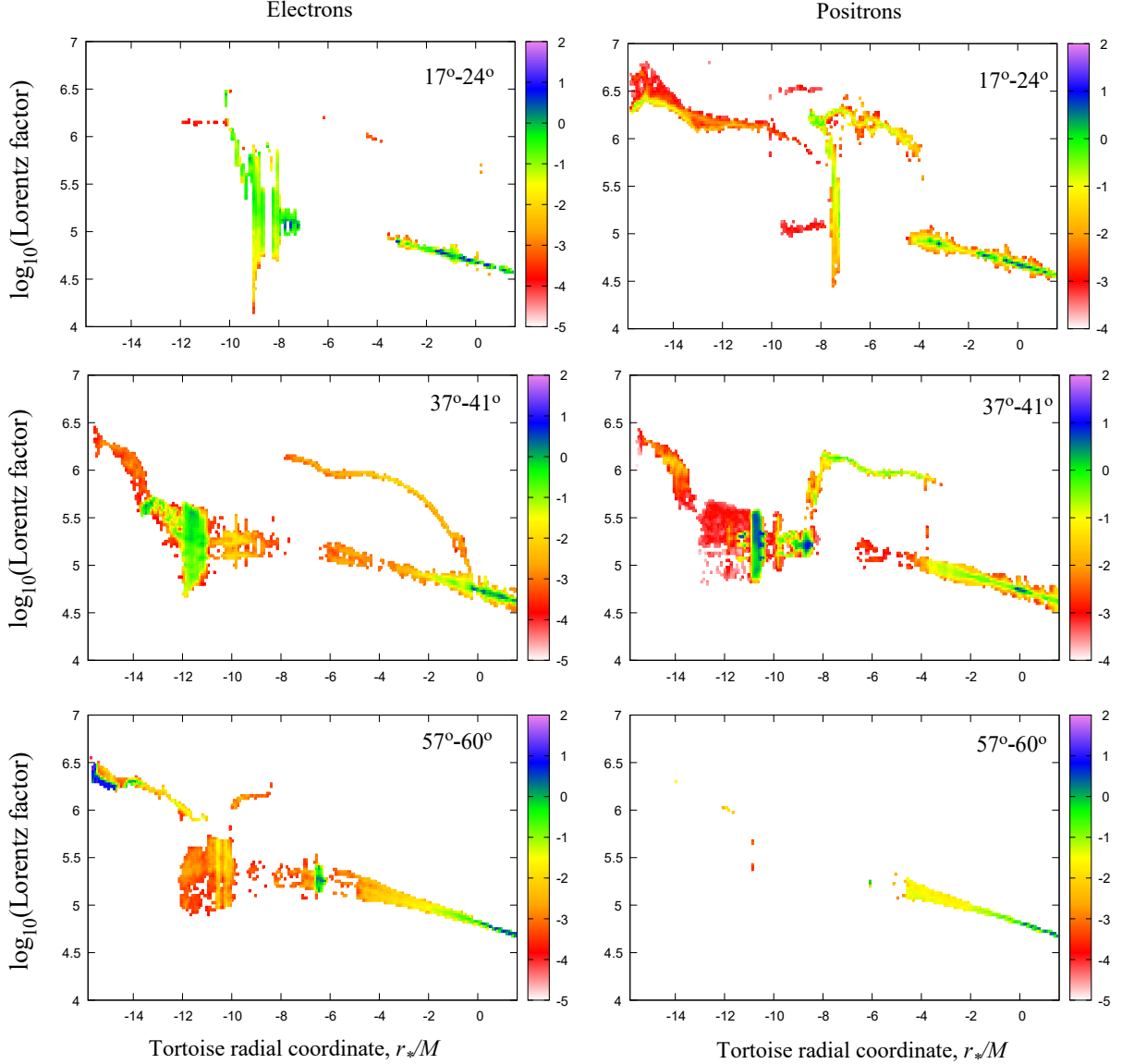


Figure 10. Lorentz factor dependence of the distribution of electrons (left) and positrons (right) as a function of the dimensionless tortoise coordinate, r_*/M , at elapsed time $t = 430M$. The color images show the logarithmic value of the dimensionless distribution functions (see text) along discrete colatitudes. The top, middle, and bottom rows show the distribution function between the meridional range $16.606^\circ - 23.568^\circ$, $37.678^\circ - 41.432^\circ$, and $57.235^\circ - 60.034^\circ$, respectively.

4.3. Comparison with previous works

Let us compare the present work with recent two works on 2-D GR PIC simulations (Parfrey et al. 2019; Crinquand et al. 2020).

First, we discuss the difference with Parfrey et al. (2019). Ignoring radiative transfer, and considering instead an injection of pairs whose rate is proportional to the local

magnetic-field-aligned electric field, they performed 2-D GR PIC simulations of the magnetospheres of an extremely rotating BH with $a = 0.999M$. The BH mass is not explicitly specified in their paper, but presumably supermassive. They adopted an extremely small magnetic field strength to emphasize the Penrose process, an energy-extraction mechanism

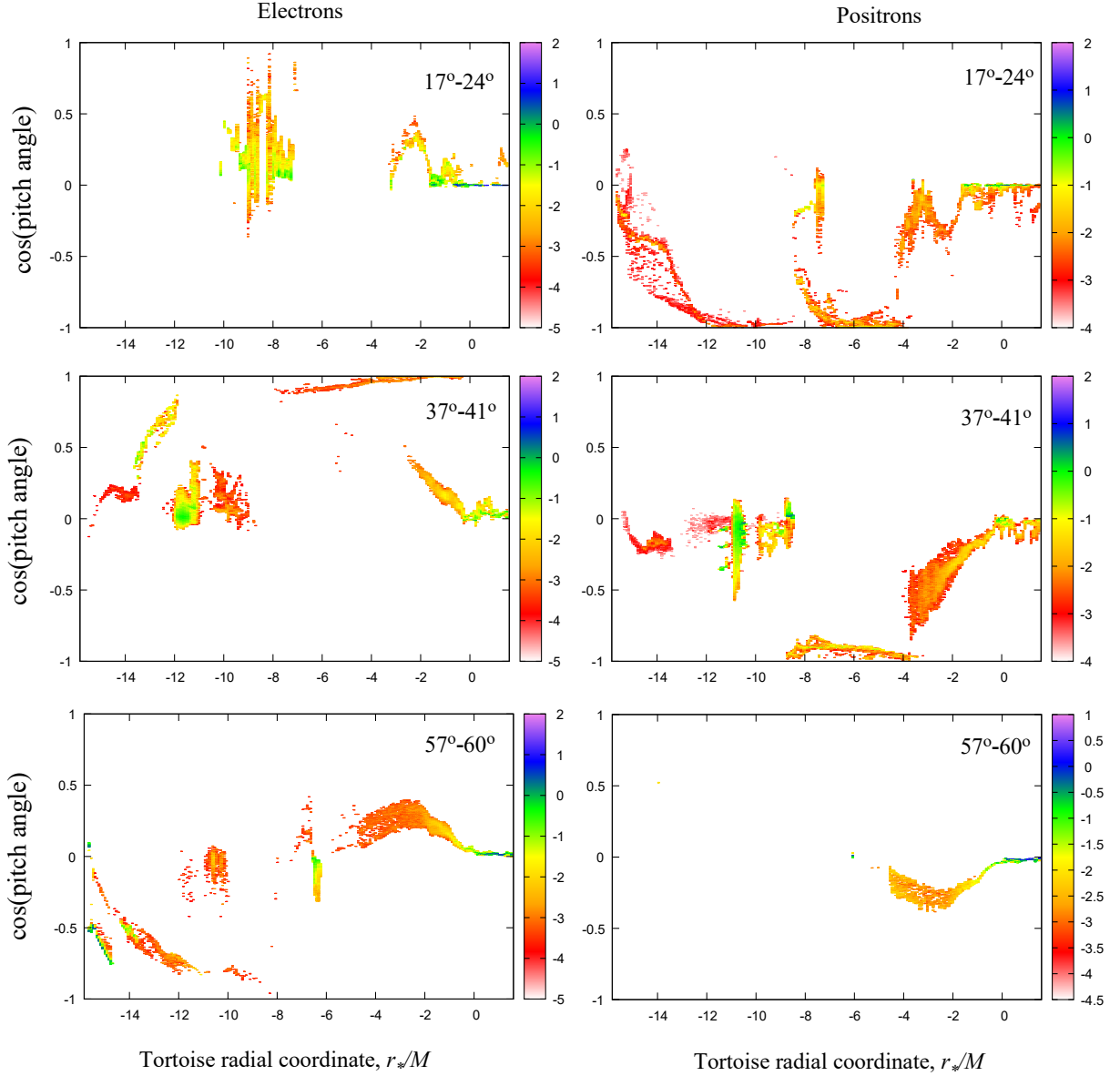


Figure 11. Similar figure as figure 10, but the pitch-angle dependence of the distribution functions of electrons (left) and positrons (right) at $t = 430M$. The color images show the logarithmic value of the dimensionless distribution functions within the same meridional range as fig. 10.

from rotating BHs when particles fall onto the horizon with negative energies measured at infinity. Particles were created in the reconnecting current sheet on the equatorial plane. The magnetization parameter was 2000; that is, the magnetosphere was still magnetically dominated. Magnetic field configuration is initially the Wald’s vacuum solution, which is produced by a toroidal ring current flowing on the equatorial plane at large distances. Then the field lines

are bend back toward the BH to penetrate the horizon. For M87*, their dimensionless magnetic field strength, $\tilde{B}_0 = 10^3$ corresponds to the actual strength $B = \tilde{B}_0(m_e c^2 / e r_g) \sim 10^{-9}$ G, which is about 10^{-11} times smaller than what is observed (Event Horizon Telescope Collaboration et al. 2019). Under this condition, they found that the charged leptons created in the current sheet plunge onto the horizon with negative energies as a result of the interaction with

the electromagnetic field, and that the Penrose process contribute in the extraction of the energy and angular momentum from a maximally rotating BH.

In the present paper, on the other hand, we consider a stellar-mass BH. In this case, we can resolve the skin depth with a realistic magnetic field strength, $B = B_{\text{eq}}$. Accordingly, the magnetization parameter becomes of the order of 10^7 ; thus, we did not mention about the particle contribution on the energy extraction from a rotating BH. Nevertheless, particle energy flux does become negative in our simulation as well; thus, the Penrose process is indeed working, although their contribution is negligible. We assume a homogeneous and constant plasma supply in the present work, which forms a contrast to Parfrey et al. (2019), who considered pair creation in the reconnecting current sheet. The magnetic field is assumed to be fixed on the poloidal plane during the simulation in the present paper.

Second, let us discuss the difference with Crinquand et al. (2020). In their 2D GR PIC code, implementing inverse-Compton scatterings (ICS) and photon-photon pair production self-consistently, they solved the PIC equations together with the radiative transfer equation. Electron-positron pair plasmas are supplied in response to gap opening. They presumed supermassive BHs. In this case, ICS dominates the pure-curvature radiation (Hirotani et al. 2016), where the particle's pitch angles become small enough due to the ICS and continuous acceleration along the magnetic field lines (Beskin et al. 1992). Thus, their treatment, which takes account of only the ICS as radiative processes, can be justified. Crinquand et al. (2020) assumed a true monopole magnetic field, whose radial component point outwards in the entire magnetosphere. Accordingly, there appear no current sheets in their solution. Electric currents flow inwards (or outwards) in the northern (or south-

ern) hemisphere, leading to a negative $F^{r\theta}$ in the entire magnetosphere. Since $E_\theta = F_{\theta t} > 0$ holds in both hemispheres, the resultant Poynting flux is also positive in both hemispheres. In their Zelton code, they solved all the six components of the electromagnetic fields, computing the evolution of $F_{\varphi t}$ from the toroidal component of the current density J^φ that is constructed from the azimuthal motion of the charged particles.

In the present paper, on the other hand, instead of solving the radiative transfer equation, we simply adopt a uniform and constant pair production in the particle source term. We consider a stellar-mass BH, in which case synchrocurvature process becomes non-negligible compared to ICS (Hirotani et al. 2016). We assume a split-monopole magnetic field, whose radial component is positive (or negative) in the northern (or southern) hemisphere. Accordingly, there appears a current sheet on the equator. Electric currents flow inwards in the higher latitudes in both hemispheres, and flow outwards in the lower latitudes, leading to a negative (or positive) $F^{r\theta}$ in the northern (or southern) hemisphere, and a positive BZ flux in both hemispheres, as discussed in §3.5.1.

Let us briefly point out the limitation of the present analysis. Unlike the Zelton code, we solved only three of the six components of the electromagnetic fields in the present paper, putting $F_{\varphi t} = 0$, and hence $\partial_t F_{\theta\varphi} = \partial_t F_{\varphi r} = 0$ throughout the simulation, as the first step. If the local physics (as supposed in recent 1-D GR PIC simulations) does not significantly affect the entire structure of the magnetosphere, such an assumption of a fixed poloidal magnetic field could be justified. However, when we apply the present 2D method to a global magnetosphere, toroidal currents carried by the charged leptons at each position can alter the entire magnetic field configuration on the poloidal plane. Thus, in the same manner as in recent 1-D models Levinson & Cerutti (2018); Chen & Yuan

(2020); Kisaka et al. (2020), we must draw attention to the limitation of $F_{\varphi t} = 0$. In the next paper, we will extend our analysis to the case $F_{\varphi t} \neq 0$, constructing J^φ at each position from the actual motion of the charged leptons, and solving all the six components of the electromagnetic fields.

4.4. Implication for supermassive black holes

Let us finally discuss what can be expected if the present results obtained for stellar-mass BHs can be applied to supermassive BHs. We have demonstrated that the BH's rotational energy is efficiently extracted along the magnetic field lines that cross the event horizon in the middle latitudes. Let us discuss an implication of this result on the formation of limb-brightened jets. It has been revealed that the innermost region of the M87 jet exhibits a limb-brightened structure by the VLBA observations in 15–43 GHz (Kovalev et al. 2007; Ly et al. 2007; Junor et al. 1999; Hada et al. 2011, 2013; Walker et al. 2018). At 86 GHz, this limb-brightened structure is already well developed at 0.15 mas from the VLBI core, where the corresponding apparent opening angle becomes approximately 100° (Hada et al. 2016). If a relatively large viewing angle of $\theta_{\text{view}} \sim 30^\circ$ is adopted (Ly et al. 2007; Hada et al. 2016), the jet has a deprojected opening angle $\chi_{\text{open}} \sim 50^\circ$ at the deprojected distance $z = 84GMc^{-2}$. However, if a smaller view angle, $\theta_{\text{view}} \sim 17^\circ$, is adopted (Biretta et al. 1999; Wang & Zhou 2009; Perlman et al. 2011; Nakamura & Meier 2014; Mertens et al. 2016; Walker et al. 2018), we obtain $\chi_{\text{open}} \sim 30^\circ$ at $z = 108GMc^{-2}$.

If a jet begins to collimate outside the outer light surface (Camenzind 1986), we may assume that the jet is radial within the distance $\zeta\varpi_{\text{LC}}$ from the rotation axis, and becomes paraboloidal outside of it (Asada & Nakamura 2012; Hada et al. 2013; Nakamura & Asada 2013; Asada et al. 2016; Nakamura et al. 2018),

where $\varpi_{\text{LC}} \equiv c/\Omega_{\text{F}}$ denotes the typical radius of the outer light surface. Figure 12 sketches the geometry of this jet downstream region. Assuming that we observe the jet at the position (r, θ) , we can express ζ in terms of the observables z and $\theta = \chi_{\text{open}}/2$ as $r(1 - \cos \theta) = (\zeta\varpi_{\text{LC}}/\sin \theta_0)(1 - \cos \theta_0)$, which gives

$$\zeta \approx \frac{z}{\varpi_{\text{LC}}} \frac{1 - \cos \theta}{\cos \theta} \frac{\sin \theta_0}{1 - \cos \theta_0}, \quad (75)$$

where $z = r \cos \theta$. If $\Omega_{\text{F}} \approx 0.5\omega_{\text{H}}$, $a \approx 0.9M$ gives $\varpi_{\text{LC}} \approx 6.4GM/c^2$. (Note that $\Omega_{\text{F}} = F_{t\theta}/F_{\theta\varphi}$ is not assumed but solved in the PIC simulation.) If the magnetic field line with the footpoint angle $\theta_0 \approx 60^\circ$ (or 75°) is brightened at downstream z with half opening angle $\theta = \chi_{\text{open}}/2$, we obtain $\zeta \approx 2.4$ (or $\zeta \approx 1.8$) for $\theta_{\text{view}} = 30^\circ$, and $\zeta \approx 1.0$ (or $\zeta \approx 0.78$) for $\theta_{\text{view}} = 17^\circ$, using the 86 GHz VLBI observations. On these grounds, if the BZ flux concentrates in the middle latitudes also around supermassive BHs, it is possible that the M87 jet begins to collimate slightly outside the outer light surface, typically within the distance $2.4\varpi_{\text{LC}}$ from the rotation axis, which may become a good target of the Event Horizon Telescope and GRAVITY.

ACKNOWLEDGMENTS

We thank the anonymous referee for careful reading and valuable comments to this manuscript. The authors acknowledge grant support to the CompAS/Antares group, and the access to high-performance computing facility from the Institute of Astronomy and Astrophysics in Academia Sinica (ASIAA). The authors acknowledge grant support from Ministry of Science and Technology (MoST) under 105-2119-M-001-044-MY3, 108-2112-M-001-009- and 109-2112-M-001-028-.

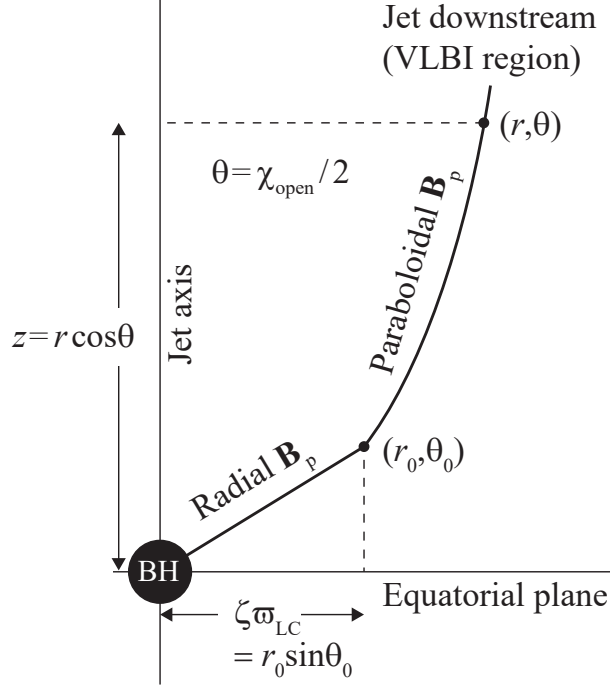


Figure 12. Schematic picture of the jet downstream region. The jet shape is assumed to be radial inside the radius r_0 , and paraboloidal outside of it. The jet is observed with VLBI at radius r . Both θ and θ_0 are measured from the jet axis, which coincides with the BH's rotation axis.

APPENDIX

A. ZAMO-MEASURED QUANTITIES

We give the expressions of ZAMO-measured quantities, which are indicated by tilde ($\tilde{}$), in this appendix section. Using equations (4)–(7), we obtain

$$u_{\tilde{r}} = \sqrt{\frac{\Delta}{\Sigma}} u_r, \quad (\text{A1})$$

$$u_{\tilde{\theta}} = \sqrt{\frac{1}{\Sigma}} u_\theta, \quad (\text{A2})$$

$$u_{\tilde{\varphi}} = \sqrt{\frac{A}{\Sigma}} \sin \theta u_\varphi, \quad (\text{A3})$$

Or equivalently, their contravariant components become

$$u_{\tilde{r}} = u^{\hat{r}} \equiv \sqrt{g_{rr}} u^r, \quad (\text{A4})$$

$$u_{\tilde{\theta}} = u^{\hat{\theta}} \equiv \sqrt{g_{\theta\theta}} u^\theta, \quad (\text{A5})$$

$$u_{\tilde{\varphi}} = u^{\hat{\varphi}} \equiv \sqrt{g_{\varphi\varphi}} (u^\varphi - \omega u^t), \quad (\text{A6})$$

$$u^j \equiv \gamma v^j, \quad (\text{A7})$$

where

$$\gamma \equiv \frac{1}{\sqrt{1 - \vec{v} \cdot \vec{v}}}. \quad (\text{A8})$$

In the same way, the tetrad transformation law gives the following expressions of the electromagnetic fields in ZAMO:

$$\begin{aligned} \tilde{E}_{\hat{r}} &= \mathbf{F}(\tilde{\mathbf{e}}_{(\hat{r})}, \tilde{\mathbf{e}}_{(\hat{t})}) \\ &= \frac{\sqrt{(r^2 + a^2)^2 - \Delta a^2 \sin^2 \theta}}{\Sigma} (F_{rt} + \omega F_{r\varphi}) \end{aligned} \quad (\text{A9})$$

$$\begin{aligned} \tilde{E}_{\hat{\theta}} &= \mathbf{F}(\tilde{\mathbf{e}}_{(\hat{\theta})}, \tilde{\mathbf{e}}_{(\hat{t})}) \\ &= \frac{\sqrt{(r^2 + a^2)^2 - \Delta a^2 \sin^2 \theta}}{\sqrt{\Delta} \Sigma} (F_{\theta t} + \omega F_{\theta\varphi}) \end{aligned} \quad (\text{A10})$$

$$\tilde{E}_{\hat{\varphi}} = \mathbf{F}(\tilde{\mathbf{e}}_{(\hat{\varphi})}, \tilde{\mathbf{e}}_{(\hat{t})}) = \frac{1}{\rho_w} F_{\varphi t} = \frac{1}{\sqrt{\Delta} \sin \theta} F_{\varphi t} \quad (\text{A11})$$

$$\tilde{B}_{\hat{r}} = {}^* \mathbf{F}(\tilde{\mathbf{e}}_{(\hat{t})}, \tilde{\mathbf{e}}_{(\hat{r})}) = F_{\hat{t}\hat{r}} = \frac{1}{\sqrt{\Sigma} g_{\varphi\varphi}} F_{\theta\varphi}, \quad (\text{A12})$$

$$\tilde{B}_{\hat{\theta}} = {}^* \mathbf{F}(\tilde{\mathbf{e}}_{(\hat{t})}, \tilde{\mathbf{e}}_{(\hat{\theta})}) = -F_{\hat{r}\hat{\theta}} = \frac{\sqrt{\Delta}}{\sqrt{\Sigma} g_{\varphi\varphi}} F_{\varphi r}, \quad (\text{A13})$$

$$\tilde{B}_{\hat{\varphi}} = {}^* \mathbf{F}(\tilde{\mathbf{e}}_{(\hat{t})}, \tilde{\mathbf{e}}_{(\hat{\varphi})}) = \sqrt{g_{rr} g_{\theta\theta}} F^{r\theta} = \frac{\Sigma}{\sqrt{\Delta}} F^{r\theta}, \quad (\text{A14})$$

where ${}^* \mathbf{F}$ refers to the Maxwell tensor, which is the dual of the Faraday tensor \mathbf{F} . For example, figure 2 depicts the distribution of equations (A12) and (A13) on the poloidal plane. We could use equations (A4) and (A5) to compute $J^{\hat{r}}$ and $J^{\hat{\theta}}$, which are depicted in figures 8–9. However, in actual calculations, we compute J^r and J^θ from equations (47) and (48) and convert them into the ZAMO-measured quantities, using the transformation law of the one-form bases that are dual to the ZAMO's tetrad, (4)–(7).

B. STATIONARY, VACUUM MAGNETOSPHERE

In this appendix section, we formulate the basic equations to solve the initial, stationary electromagnetic fields.

B.1. *The Gauss's law*

The inhomogeneous part of the Maxwell equations can be written as

$$\nabla_{\mu} F^{\nu\mu} = \frac{4\pi}{c} J^{\nu}, \quad (\text{B15})$$

where ∇_{μ} denotes the covariant derivative with respect to the coordinate variable x^{μ} , $F^{\nu\mu}$ the electromagnetic field strength tensor, and J^{ν} the four current density. Putting $\nu = 0$, we obtain the Gauss's law,

$$\frac{1}{\sqrt{-g}} \partial_{\mu} (\sqrt{-g} F^{0\mu}) = 4\pi\rho, \quad (\text{B16})$$

where ρ refers to the electric charge density, and $\sqrt{-g} = \Sigma \sin \theta$. In the Kerr spacetime, we obtain

$$F^{01} = F^{tr} = \frac{g^{rr}}{\rho_w^2} (-g_{\varphi\varphi} F_{tr} + g_{t\varphi} F_{\varphi r}), \quad (\text{B17})$$

$$F^{02} = F^{t\theta} = \frac{g^{\theta\theta}}{\rho_w^2} (-g_{\varphi\varphi} F_{t\theta} + g_{t\varphi} F_{\varphi\theta}), \quad (\text{B18})$$

$$F^{03} = F^{t\varphi} = \frac{1}{\rho_w^2} F_{\varphi t} \quad (\text{B19})$$

At $t = 0$, we assume stationary and axisymmetric magnetosphere, $\partial_t = \partial_{\varphi} = 0$, to obtain

$$F_{rt} = A_{t,r} - A_{r,t} = A_{t,r} = \partial_r A_t, \quad (\text{B20})$$

$$F_{\theta t} = A_{t,\theta} - A_{\theta,t} = A_{t,\theta} = \partial_{\theta} A_t, \quad (\text{B21})$$

$$F_{\varphi t} = A_{t,\varphi} - A_{\varphi,t} = 0, \quad (\text{B22})$$

$$F_{\varphi r} = A_{r,\varphi} - A_{\varphi,r} = -\partial_r A_{\varphi}, \quad (\text{B23})$$

$$F_{\theta\varphi} = A_{\varphi,\theta} - A_{\theta,\varphi} = \partial_{\theta} A_{\varphi}, \quad (\text{B24})$$

where $A_{\mu} = (A_t, A_r, A_{\theta}, A_{\varphi})$ denotes the vector potential; $F_{\mu\nu} = \partial_{\mu} A_{\nu} - \partial_{\nu} A_{\mu}$. Note that $F_{r\theta,\varphi} + F_{\theta\varphi,r} + F_{\varphi r,\theta} = 0$ (i.e., $\nabla \cdot \mathbf{B} = 0$) is automatically satisfied.

For an observer whose four velocity is u^{ν} , the electromagnetic field components are given by

$$E_{\mu} = F_{\mu\nu} u^{\nu}, \quad (\text{B25})$$

and

$$B^{\mu} = \frac{1}{2} \eta_{\nu}^{\mu\rho\sigma} F_{\rho\sigma} u^{\nu}, \quad (\text{B26})$$

where the completely anti-symmetric, Levi-Civita tensor density is defined by

$$\eta_{\nu\mu\rho\sigma} = -\eta_{\mu\nu\rho\sigma} = -\eta_{\rho\mu\nu\sigma} = -\eta_{\sigma\mu\rho\nu} = -\eta_{\nu\rho\mu\sigma} = -\eta_{\nu\sigma\rho\mu} = -\eta_{\nu\mu\sigma\rho} \quad (\text{B27})$$

and

$$\eta_{tr\theta\varphi} = -\frac{1}{\eta^{tr\theta\varphi}} = \sqrt{-g}. \quad (\text{B28})$$

Thus, for a distant static observer whose four velocity is $\xi^{\mu} = (1, 0, 0, 0)$, that is, the time-like Killing vector, the electric field components are obtained by

$$E_r = F_{rt}, \quad E_{\theta} = F_{\theta t}, \quad E_{\varphi} = F_{\varphi t} \quad (\text{B29})$$

in the Boyer-Lindquist coordinate. The magnetic field becomes

$$\begin{aligned} B^r &= \frac{-g_{tt}F_{\theta\varphi} + g_{t\varphi}F_{\theta t}}{\sqrt{-g}}, \\ B^\theta &= \frac{-g_{tt}F_{\varphi r} + g_{t\varphi}F_{rt}}{\sqrt{-g}}, \\ B_\varphi &= -\sqrt{-g}F^{r\theta}. \end{aligned} \quad (\text{B30})$$

Substituting equations (B20), (B21), (B23) and (B24) into equation (B16), we obtain the Gauss's law:

$$\begin{aligned} \frac{1}{\Sigma} \frac{\partial}{\partial r} \left(\frac{A}{\Sigma} \frac{\partial A_t}{\partial r} \right) + \frac{1}{\Delta \Sigma \sin \theta} \frac{\partial}{\partial \theta} \left(\frac{A}{\Sigma} \sin \theta \frac{\partial A_t}{\partial \theta} \right) + \frac{1}{\Sigma} \frac{\partial}{\partial r} \left(\frac{2Mar}{\Sigma} \frac{\partial A_\varphi}{\partial r} \right) \\ + \frac{1}{\Delta \Sigma \sin \theta} \frac{\partial}{\partial \theta} \left(\frac{2Mar}{\Sigma} \sin \theta \frac{\partial A_\varphi}{\partial \theta} \right) = 4\pi\rho. \end{aligned} \quad (\text{B31})$$

It follows that this Poisson equation contains only A_t (i.e., the scalar potential) if the BH is non-rotating (i.e., $a = 0$). However, around a rotating BH (i.e., if $a \neq 0$), A_φ comes into the Gauss's law. We thus need one more differential equation that contains both A_t and A_φ .

B.2. The Biot and Savart law

To obtain an independent constraint on A_t and A_φ , we consider the Biot and Savart law. Putting $\nu = \varphi$ in equation (B15), we obtain

$$\frac{1}{\sqrt{-g}} \partial_\mu (\sqrt{-g} F^{\varphi\mu}) = \frac{4\pi}{c} J^\varphi, \quad (\text{B32})$$

Thus, equations (B17)–(B24) give

$$\begin{aligned} -\frac{1}{\sin \theta} \frac{\partial}{\partial r} \left(\frac{\Delta - a^2 \sin^2 \theta}{\Sigma} \frac{\partial A_\varphi}{\partial r} \right) - \frac{1}{\Delta} \frac{\partial}{\partial \theta} \left(\frac{\Delta - a^2 \sin^2 \theta}{\Sigma \sin \theta} \frac{\partial A_\varphi}{\partial \theta} \right) \\ + \frac{\partial}{\partial r} \left(\frac{2Mar \sin \theta}{\Sigma} \frac{\partial A_t}{\partial r} \right) + \frac{1}{\Delta} \frac{\partial}{\partial \theta} \left(\frac{2Mar \sin \theta}{\Sigma} \frac{\partial A_t}{\partial \theta} \right) = 4\pi \Sigma \sin \theta J^\varphi, \end{aligned} \quad (\text{B33})$$

where $c = 1$ is used. It follows that this equation contains only A_φ (i.e., the azimuthal component of the vector potential) if $a = 0$. However, if $a \neq 0$, we must simultaneously solve the two second-order partial differential equations (B31) and (B33) for A_t and A_φ .

It should be noted that the coefficients of the $\partial_r^2 A_\varphi$ and the $\partial_\theta^2 A_\varphi$ terms in equation (B33) change sign at the static limit, where g_{tt} vanishes. Since the coefficients of these two highest-order derivative terms change sign with respect to those of the other two highest-order derivative terms (i.e., the $\partial_r^2 A_t$ and the $\partial_\theta^2 A_t$ terms), the solution diverges during iterations from the inside of the static limit (i.e., within the so-called “ergosphere”) if we impose boundary conditions in the same way as standard elliptic type partial differential equations. This ill behaviour is incurred because a static observer (with respect to the star) becomes unphysical within the ergosphere.

There are many ways to overcome this ill behaviour. In the present paper, we solve this issue by adopting the ZAMO as a physical observer. Using the ZAMO's tetrad, equations (4)–(7), we can replace A_t with the ZAMO-measured scalar potential, $A_{\hat{t}}$ (eq. [12]), and obtain the two elliptic-type equations (14) and (19), which describe the initial electromagnetic fields at $t = 0$.

C. PAIR PRODUCTION RATE

Using the self-similar analytical solution of Newtonian ADAF model (Mahadevan 1997), we find that the photons are emitted at the rate

$$q_{\text{ff}} = 1.8 \times 10^2 \theta_e \dot{m}^2 M_9^{-2} \left(\frac{r}{2M} \right)^{-3} \text{ ergs s}^{-1} \text{ cm}^{-3} \quad (\text{C34})$$

by Bremsstrahlung, where $\theta_e \equiv kT_e/m_e c^2$ denotes the dimensionless electron temperature. The luminosity of this Bremsstrahlung emission can be computed as

$$L_{\text{ff}}(r) = 2\pi \int_{\theta_1}^{\theta_2} \int_{r_{\text{min}}}^r q_{\text{ff}}(r) r^2 \sin \theta dr d\theta \approx 2\pi \times 1.8 \times 10^2 \theta_e \dot{m}^2 M_9^{-2} (2M)^3 \ln \left(\frac{r}{2M} \right), \quad (\text{C35})$$

where $\theta_1 \sim 60^\circ$ and $\theta_2 \sim 120^\circ$ denote the upper and lower boundary colatitudes of the ADAF.

In general, if one photon species (e.g., ADAF Bremsstrahlung photons or gap-emitted gamma-rays) collide with another photon species (e.g., ADAF Bremsstrahlung photons or ADAF synchrotron photons), the pair production rate is given by

$$\dot{n}_{\pm}(r) = \int d\nu_{\gamma} \alpha_{\gamma\gamma} \frac{1}{c} \int \frac{I_{\nu}}{h\nu} d\Omega_{\gamma}, \quad (\text{C36})$$

where $d\Omega_{\gamma}$ refers to the photon propagation solid angle, and

$$\alpha_{\gamma\gamma} = (1 - \mu) \int_{\epsilon_{\text{th}}}^{\infty} \frac{dF_{\gamma}}{d\epsilon_{\gamma}} \sigma_{\gamma\gamma} d\epsilon_{\gamma} \approx (1 - \mu) F_{\gamma} \sigma_{\gamma\gamma} \quad (\text{C37})$$

denotes the photon-photon absorption coefficient, and

$$F_{\gamma} \equiv \int d\nu_{\gamma} \int \frac{I_{\nu}}{h\nu} d\Omega_{\gamma} \quad (\text{C38})$$

denotes the photon number flux; I_{ν} , ν_{γ} and μ show the specific intensity, photon frequency, and the cosine of the photon collision angles, respectively.

In the present case, the two species are the same ADAF Bremsstrahlung photons. Thus, we obtain

$$\dot{n}_{\pm}(r) \approx (1 - \mu) \sigma_{\gamma\gamma} \frac{F_{\gamma}^2}{c} \quad (\text{C39})$$

Evaluating the flux with the luminosity by

$$F_{\gamma}(r) \approx \frac{L_{\text{ff}}(r)}{2\pi r^2 \epsilon_{\gamma}}, \quad (\text{C40})$$

where the photon energy can be estimated to be $\epsilon_{\gamma} \approx 3\theta_e m_e c^2$, and assuming that the pair production rate is uniform within $r < 4M$, we obtain equation (51), where the relative velocity factor is evaluated as $1 - \mu = 0.2$, and the pair-production cross section as the 20% of the Thomson cross section, $\sigma_{\gamma\gamma} = 0.2\sigma_{\text{T}}$.

D. COVARIANCE OF THE RADIATION-REACTION FORCE

We explain here that the radiation reaction force contains not only those obtained in a flat space (Cerutti et al. 2012, 2013),

$$P_{\text{rad,flat}} = \frac{2}{3}e^2c\frac{q^2}{m^2}\gamma^2 \left[-\left(\frac{\mathbf{v}}{c} \cdot \tilde{\mathbf{E}}\right)^2 + \left(\tilde{\mathbf{E}} + \frac{\mathbf{v}}{c} \times \tilde{\mathbf{B}}\right)^2 \right], \quad (\text{D41})$$

in locally homogeneous $\tilde{\mathbf{E}}$ and $\tilde{\mathbf{B}}$ fields, but also contains the power of radiative processes that result from any kinds of acceleration. To find this, we write down equations (44) in a covariant form,

$$\frac{du^\mu}{d\lambda} = -\Gamma^\mu_{\rho\sigma}u^\rho u^\sigma + \frac{q}{m}F^\mu_{\rho}u^\rho, \quad (\text{D42})$$

where the friction term is dropped here in the right-hand side to draw the conclusion from the first principles. Both the inertial forces (e.g., the centrifugal and the Coriolis forces) and the gravitational forces (due to the spacetime curvature) are included in the connection coefficients, $\Gamma^\mu_{\rho\sigma}$. For example, when a charge (or its guiding center) moves along a curved magnetic field line in a flat space, we can introduce a local cylindrical (or polar) coordinate system whose origin resides at the center of the curved path of 3D particle motion. In this coordinate, the $\Gamma^\mu_{\rho\sigma}u^\rho u^\sigma$ term gives the centripetal acceleration, $a_\perp = c^2/R_c$, where R_c refers to the curvature radius of the 3D particle motion. Since equation (46) is covariant, the effect of such curvature radiation is included in any frame of reference. Accordingly, we can take account of radiation effects due to any acceleration. Note that a charged particle does radiate by gravitational acceleration irrespective of the frame of reference.

In actual program, we can compute the radiation-reaction force F_{rad}^j iteratively. Namely, (1) we first set $F_{\text{rad}}^j = 0$ and update $du^j/d\lambda$ and $du^0/d\lambda = \gamma$ by equation (44), (2) second, we substitute the solved u^μ in equation (46) to update F_{rad}^j , (3) third, use the updated F_{rad}^j and solve equation (44) for u^μ again, (4) iterate steps (2) and (3) until F_{rad}^j saturates. If we use the F_{rad}^j obtained in the previous step for each particle and start from step (3), the number of iterations can be reduced.

E. DISCRETIZATION OF BASIC EQUATIONS

We discretize the Maxwell equations (35)–(37) adopting the Yee lattice. Electric field components, E and D , are evaluated at half integer time steps, e.g., at $t \pm (1/2)\Delta_t$, and the magnetic field component, B , is evaluated at integer time step at time $t + \Delta_t$. Accordingly, equations (35)–(37) are discretized as follows:

$$\begin{aligned} & B^{n+1}_{i+1/2,j+1/2} - B^n_{i+1/2,j+1/2} \\ &= -c_1\nu_x \left(E^{n+1/2}_{i+1,j+1/2} - E^{n+1/2}_{i,j+1/2} \right) + c_2\nu_y \left(D^{n+1/2}_{i+1/2,j+1} - D^{n+1/2}_{i+1/2,j} \right), \end{aligned} \quad (\text{E43})$$

$$\begin{aligned} & D^{n+1/2}_{i+1/2,j} - D^{n-1/2}_{i+1/2,j} \\ &= c_3\nu_y \left(B^n_{i+1/2,j+1/2} - B^n_{i+1/2,j-1/2} \right) - 4\pi(\Delta_t) \frac{\Sigma^2}{A} \Big|_{i+1/2,j} (J^r)_{i+1/2,j}^n, \end{aligned} \quad (\text{E44})$$

$$\begin{aligned} & E^{n+1/2}_{i,j+1/2} - E^{n-1/2}_{i,j+1/2} \\ &= -c_4\nu_x \left(B^n_{i+1/2,j+1/2} - B^n_{i-1/2,j+1/2} \right) - 4\pi(\Delta_t) \frac{\Sigma^2\Delta \sin\theta}{A} \Big|_{i+1/2,j} (J^\theta)_{i,j+1/2}^n, \end{aligned} \quad (\text{E45})$$

where the super- and sub-scripts denote the temporal and spatial labels, respectively; and the Courant numbers are defined by

$$\nu_x \equiv \frac{\Delta_t}{\Delta_x}, \quad (\text{E46})$$

$$\nu_y \equiv \frac{\Delta_t}{\Delta_y}. \quad (\text{E47})$$

Here, Δ_t denotes the time step, Δ_x denotes the constant interval of the radial tortoise coordinate, and $\Delta_y = \sin \theta \Delta_\theta$ denotes the constant azimuthal grid interval. Denoting the inner and outer boundary positions as r_*^{\min} and r_*^{\max} , we obtain $\Delta_x = (r_*^{\max} - r_*^{\min}) / (N_x - 1)$, where N_x denotes the number of radial grids. Since we consider the colatitudes range $0 < 1 - \cos \theta < 2$, we obtain $\Delta_y = 2 / (N_y - 1)$, where N_y denotes the number of meridional grids.

As for the Hamilton-Jacobi equations (44) and (47)–(49), we evaluate the particle position (r, θ, φ) at half integer time steps, and the momentum $(u^r, u^\theta, u^\varphi, \text{ and } \gamma)$ at integer time steps. Namely, particle's momentum evolves by (eq. [44])

$$\mathbf{u}^{n+1} - \mathbf{u}^n = (\Delta_t) \mathbf{F}(t^{n+1/2}, \mathbf{x}^{n+1/2}, \mathbf{u}^{n+1/2}), \quad (\text{E48})$$

where F_i represents the right-hand side of equation (44).

On the other hand, particle's position evolves by (eq. [47]–[49])

$$r^{n+1/2} = r^{n-1/2} + \left(\frac{u^r}{u^t} \right)^n, \quad (\text{E49})$$

$$\theta^{n+1/2} = \theta^{n-1/2} + \left(\frac{u^\theta}{u^t} \right)^n, \quad (\text{E50})$$

$$\varphi^{n+1/2} = \varphi^{n-1/2} + \left(\frac{u^\varphi}{u^t} \right)^n \quad (\text{E51})$$

The Boyer-Lindquist radial coordinate r can be readily converted into $x = r_*$ by equation (10), whereas θ is related to y by $y = 1 - \cos \theta$.

To find the initial, stationary solution, we divide the tortoise coordinate x uniformly between $-15.8180 < x < 20.0000$, and the meridional coordinate y uniformly between $0 < y = 1 - \cos \theta < 2$. Accordingly, the Boyer-Lindquist coordinates are divided non-uniformly as $r_1 = 1.4651M$, $r_2 = 1.4656M$, $r_3 = 1.4662M$, \dots , $r_{599} = 19.9462M$, $r_{600} = 20.0000M$, and $\theta_1 = 0^\circ$, $\theta_2 = 2.6160^\circ$, $\theta_3 = 3.7000^\circ$, $\theta_4 = 4.5319^\circ$, \dots , $\theta_{959} = 89.9104^\circ$, $\theta_{960} = 89.9701^\circ$, $\theta_{961} = 90.0298^\circ$, \dots , $\theta_{1918} = (180.0000 - 3.7000)^\circ$, $\theta_{1919} = (180.0000 - 2.6160)^\circ$, $\theta_{1920} = 180.0000^\circ$.

To perform PIC simulations, we must restrict the radial range small compared to the stationary case, because the Gauss's and Biot-Savart laws are solved for the toroidal current distribution within $r < 20M$, which makes the solved poloidal electromagnetic fields be accurate typically only within $r < 14M$. The actual value of the right-hand side (i.e., $14M$ in this case) depends on the r dependence of J^φ_{eq} . For a split-monopole case, $J^\varphi_{\text{eq}} \propto r^{-4}$, or a paraboloidal case, $J^\varphi_{\text{eq}} \propto r^{-3}$, the outer radial boundary of $r \sim 14M$ is conservatively justified. For PIC simulations, we thus adopt the inner 960 points to restrict the simulation range within $x_1 = -15.8180 < x < x_{960} = 12.8244$, or equivalently, $r_1 = 1.4646M < r < r_{960} = 13.6854M$. For meridional coordinate y , and adopt the same gridding as in the stationary case. We checked that the results little change when we halve the resolution either in radial or meridional direction, or when we halve the creation rate $1/k_{\text{create}}$ (and hence the number of particles per cell).

F. CURRENT DEPOSIT

In our present 2D PIC simulations, we adopt a grid consisting of rectangles of unit size, and place on it unit rectangular charges, where each unit rectangle grid cell has an area $\Delta_x\Delta_y$ (Appendix E). The total amount of charges is assumed to be the uniformly distributed over its 2D surface. As a charge moves, each grid cell boundary sweeps a fraction of the particle's unit area surface, giving the electric current flowing across the boundary. Using this 'area weighting' (Villasenor & Buneman 1992), we sum up the currents carried by individual particles on each grid boundary.

We should notice here that we take account of the particle motion only in the poloidal plane when we compute the current density, although the particles' EOM is solved three-dimensionally. Thus, we cannot compute the toroidal current density, J^φ , in our area weighting method. It follows that the time evolution of E_φ cannot be solved from the Ampere's law. Accordingly, the evolution of B^r or B^θ cannot be solved either, because r and θ components of the Faraday law contain $\partial_\theta E_\varphi$ and $\partial_r E_\varphi$, respectively. Thus, we are able to solve only the three components (i.e., B , D , and E) of the electromagnetic field by equations (35)–(37) in the present 2D scheme, unless J^φ is constructed from particle's toroidal motion by a 'volume weighting' method, which is out of the scope of the present paper.

REFERENCES

- Asada, K., & Nakamura, M. 2012, *ApJL*, 745, L28, doi: [10.1088/2041-8205/745/2/L28](https://doi.org/10.1088/2041-8205/745/2/L28)
- Asada, K., Nakamura, M., & Pu, H.-Y. 2016, *ApJ*, 833, 56, doi: [10.3847/1538-4357/833/1/56](https://doi.org/10.3847/1538-4357/833/1/56)
- Bacchini, F., Ripperda, B., Chen, A. Y., & Sironi, L. 2018, *ApJS*, 237, 6, doi: [10.3847/1538-4365/aac9ca](https://doi.org/10.3847/1538-4365/aac9ca)
- Bardeen, J. M. 1970, *Nature*, 226, 64, doi: [10.1038/226064a0](https://doi.org/10.1038/226064a0)
- Beskin, V. S., Istomin, Y. N., & Pavlov, V. I. 1992, *Soviet Ast.*, 36, 642
- Biretta, J. A., Sparks, W. B., & Macchetto, F. 1999, *ApJ*, 520, 621, doi: [10.1086/307499](https://doi.org/10.1086/307499)
- Blandford, R. D., & Znajek, R. L. 1977, *MNRAS*, 179, 433, doi: [10.1093/mnras/179.3.433](https://doi.org/10.1093/mnras/179.3.433)
- Bohdan, A., Niemiec, J., Pohl, M., et al. 2019, *ApJ*, 885, 10, doi: [10.3847/1538-4357/ab43cf](https://doi.org/10.3847/1538-4357/ab43cf)
- Boyer, R. H., & Lindquist, R. W. 1967, *Journal of Mathematical Physics*, 8, 265, doi: [10.1063/1.1705193](https://doi.org/10.1063/1.1705193)
- Camenzind, M. 1986, *A&A*, 162, 32
- Cerutti, B., Uzdensky, D. A., & Begelman, M. C. 2012, *ApJ*, 746, 148, doi: [10.1088/0004-637X/746/2/148](https://doi.org/10.1088/0004-637X/746/2/148)
- Cerutti, B., Werner, G. R., Uzdensky, D. A., & Begelman, M. C. 2013, *ApJ*, 770, 147, doi: [10.1088/0004-637X/770/2/147](https://doi.org/10.1088/0004-637X/770/2/147)
- Chen, A. Y., & Yuan, Y. 2020, *ApJ*, 895, 121, doi: [10.3847/1538-4357/ab8c46](https://doi.org/10.3847/1538-4357/ab8c46)
- Chen, A. Y., Yuan, Y., & Yang, H. 2018, *ApJL*, 863, L31, doi: [10.3847/2041-8213/aad8ab](https://doi.org/10.3847/2041-8213/aad8ab)
- Crinquand, B., Cerutti, B., Philippov, A. e., Parfrey, K., & Dubus, G. 2020, *PhRvL*, 124, 145101, doi: [10.1103/PhysRevLett.124.145101](https://doi.org/10.1103/PhysRevLett.124.145101)
- Event Horizon Telescope Collaboration, Akiyama, K., Alberdi, A., et al. 2019, *ApJL*, 875, L5, doi: [10.3847/2041-8213/ab0f43](https://doi.org/10.3847/2041-8213/ab0f43)
- Ferrarese, L., Ford, H. C., & Jaffe, W. 1996, *ApJ*, 470, 444, doi: [10.1086/177876](https://doi.org/10.1086/177876)
- Hada, K., Doi, A., Kino, M., et al. 2011, *Nature*, 477, 185, doi: [10.1038/nature10387](https://doi.org/10.1038/nature10387)
- Hada, K., Kino, M., Doi, A., et al. 2013, *ApJ*, 775, 70, doi: [10.1088/0004-637X/775/1/70](https://doi.org/10.1088/0004-637X/775/1/70)
- . 2016, *ApJ*, 817, 131, doi: [10.3847/0004-637X/817/2/131](https://doi.org/10.3847/0004-637X/817/2/131)
- Hirose, S., Krolik, J. H., De Villiers, J.-P., & Hawley, J. F. 2004, *ApJ*, 606, 1083, doi: [10.1086/383184](https://doi.org/10.1086/383184)
- Hirovani, K., & Okamoto, I. 1998, *ApJ*, 497, 563, doi: [10.1086/305479](https://doi.org/10.1086/305479)
- Hirovani, K., & Pu, H.-Y. 2016, *ApJ*, 818, 50, doi: [10.3847/0004-637X/818/1/50](https://doi.org/10.3847/0004-637X/818/1/50)
- Hirovani, K., Pu, H.-Y., Lin, L. C.-C., et al. 2016, *ApJ*, 833, 142, doi: [10.3847/1538-4357/833/2/142](https://doi.org/10.3847/1538-4357/833/2/142)

- Hughes, S. A., Keeton, Charles R., I., Walker, P., et al. 1994, *PhRvD*, 49, 4004, doi: [10.1103/PhysRevD.49.4004](https://doi.org/10.1103/PhysRevD.49.4004)
- Ichimaru, S. 1977, *ApJ*, 214, 840, doi: [10.1086/155314](https://doi.org/10.1086/155314)
- Jackson, J. D. 1962, *Classical Electrodynamics*
- Junor, W., Biretta, J. A., & Livio, M. 1999, *Nature*, 401, 891, doi: [10.1038/44780](https://doi.org/10.1038/44780)
- Kisaka, S., Levinson, A., & Toma, K. 2020, arXiv e-prints, arXiv:2007.02838, <https://arxiv.org/abs/2007.02838>
- Koide, S., Shibata, K., Kudoh, T., & Meier, D. L. 2002, *Science*, 295, 1688, doi: [10.1126/science.1068240](https://doi.org/10.1126/science.1068240)
- Kormendy, J., & Ho, L. C. 2013, *ARA&A*, 51, 511, doi: [10.1146/annurev-astro-082708-101811](https://doi.org/10.1146/annurev-astro-082708-101811)
- Kovalev, Y. Y., Lister, M. L., Homan, D. C., & Kellermann, K. I. 2007, *ApJL*, 668, L27, doi: [10.1086/522603](https://doi.org/10.1086/522603)
- Larkin, A. C., & McLaughlin, D. E. 2016, *MNRAS*, 462, 1864, doi: [10.1093/mnras/stw1749](https://doi.org/10.1093/mnras/stw1749)
- Levinson, A., & Cerutti, B. 2018, *A&A*, 616, A184, doi: [10.1051/0004-6361/201832915](https://doi.org/10.1051/0004-6361/201832915)
- Levinson, A., & Rieger, F. 2011, *ApJ*, 730, 123, doi: [10.1088/0004-637X/730/2/123](https://doi.org/10.1088/0004-637X/730/2/123)
- Ly, C., Walker, R. C., & Junor, W. 2007, *ApJ*, 660, 200, doi: [10.1086/512846](https://doi.org/10.1086/512846)
- Mahadevan, R. 1997, *ApJ*, 477, 585, doi: [10.1086/303727](https://doi.org/10.1086/303727)
- McKinney, J. C., & Narayan, R. 2007, *MNRAS*, 375, 513, doi: [10.1111/j.1365-2966.2006.11301.x](https://doi.org/10.1111/j.1365-2966.2006.11301.x)
- McKinney, J. C., Tchekhovskoy, A., & Blandford, R. D. 2012, *MNRAS*, 423, 3083, doi: [10.1111/j.1365-2966.2012.21074.x](https://doi.org/10.1111/j.1365-2966.2012.21074.x)
- Mertens, F., Lobanov, A. P., Walker, R. C., & Hardee, P. E. 2016, *A&A*, 595, A54, doi: [10.1051/0004-6361/201628829](https://doi.org/10.1051/0004-6361/201628829)
- Nakamura, M., & Asada, K. 2013, *ApJ*, 775, 118, doi: [10.1088/0004-637X/775/2/118](https://doi.org/10.1088/0004-637X/775/2/118)
- Nakamura, M., & Meier, D. L. 2014, *ApJ*, 785, 152, doi: [10.1088/0004-637X/785/2/152](https://doi.org/10.1088/0004-637X/785/2/152)
- Nakamura, M., Asada, K., Hada, K., et al. 2018, *ApJ*, 868, 146, doi: [10.3847/1538-4357/aaeb2d](https://doi.org/10.3847/1538-4357/aaeb2d)
- Narayan, R., & Yi, I. 1994, *ApJL*, 428, L13, doi: [10.1086/187381](https://doi.org/10.1086/187381)
- Neronov, A., & Aharonian, F. A. 2007, *ApJ*, 671, 85, doi: [10.1086/522199](https://doi.org/10.1086/522199)
- Parfrey, K., Philippov, A., & Cerutti, B. 2019, *PhRvL*, 122, 035101, doi: [10.1103/PhysRevLett.122.035101](https://doi.org/10.1103/PhysRevLett.122.035101)
- Perlman, E. S., Adams, S. C., Cara, M., et al. 2011, *ApJ*, 743, 119, doi: [10.1088/0004-637X/743/2/119](https://doi.org/10.1088/0004-637X/743/2/119)
- Tanabe, K., & Nagataki, S. 2008, *PhRvD*, 78, 024004, doi: [10.1103/PhysRevD.78.024004](https://doi.org/10.1103/PhysRevD.78.024004)
- Tchekhovskoy, A., Narayan, R., & McKinney, J. C. 2010, *ApJ*, 711, 50, doi: [10.1088/0004-637X/711/1/50](https://doi.org/10.1088/0004-637X/711/1/50)
- Thorne, K. S., & MacDonald, D. 1982, *MNRAS*, 198, 339, doi: [10.1093/mnras/198.2.339](https://doi.org/10.1093/mnras/198.2.339)
- Villasenor, J., & Buneman, O. 1992, *Computer Physics Communications*, 69, 306, doi: [10.1016/0010-4655\(92\)90169-Y](https://doi.org/10.1016/0010-4655(92)90169-Y)
- Walker, R. C., Hardee, P. E., Davies, F. B., Ly, C., & Junor, W. 2018, *ApJ*, 855, 128, doi: [10.3847/1538-4357/aaafcc](https://doi.org/10.3847/1538-4357/aaafcc)
- Wang, C.-C., & Zhou, H.-Y. 2009, *MNRAS*, 395, 301, doi: [10.1111/j.1365-2966.2009.14463.x](https://doi.org/10.1111/j.1365-2966.2009.14463.x)
- Yuan, F., & Narayan, R. 2014, *ARA&A*, 52, 529, doi: [10.1146/annurev-astro-082812-141003](https://doi.org/10.1146/annurev-astro-082812-141003)